K^+ momentum spectrum from (K^-, K^+) reactions in intranuclear cascade model

Y. Nara[a1], A. Ohnishi[a,b], T. Harada[c] and A. Engel[d]

a. *Department of Physics, Faculty of Science, Hokkaido University, Sapporo 060, Japan*
b. *Nuclear Science Division, Lawrence Berkeley Laboratory, Berkeley, CA 94720, USA*
c. *Department of Social Information, Sapporo Gakuin University, Ebetsu 069, Japan*
d. *Department of Physics, Kyoto University, Kyoto, 606-01, Japan*

Abstract

In a framework of intranuclear cascade (INC) type calculation, we study a momentum spectrum in reactions (K^-, K^+) at a beam momentum of 1.65 GeV/c. INC model calculations are compared with the relativistic impulse approximation (RIA) calculations to perform the detailed study of the reaction mechanism. We find that the INC model can reproduce the experimental data on various targets. Especially, in the low-momentum region, the forward-angle cross sections of the (K^-, K^+) reaction on from light to heavy targets are consistently explained with the two-step strangeness exchange and production processes with various intermediate mesons, and ϕ, a_0 and f_0 productions and their decay into $K^+ K^-$. In the two-step processes, inclusion of meson and hyperon resonances is found to be essential.

1   Introduction

The study of nuclear systems with strangeness $S = -2$ is one of the most important and hottest subjects in nuclear physics, since these systems give us unique information on YY interaction and they might be a doorway to study multi-strangeness systems such as the strange matter. Until now, several ways to produce these $S = -2$ nuclear systems have been proposed [1].

The first one is the Ξ^- absorption reaction at rest on nuclei. In these thirty years, there are three reports on the discovery of double-hypernuclei through the Ξ^- absorption. These events are found in the emulsion by searching for the sequential weak decay processes (double stars) [2]. Although the Ξ^- absorption reaction is the most effective and the most direct way for the double-hypernucleus hunting, it is necessary to produce slow Ξ^- particles, to stop them in the emulsion, and to search for the double stars in the emulsion. Thus the information is still too scarce to determine YY interaction at present, and further study along this line is necessary. The second way to produce $S = -2$ nuclear systems is the production of double-hypernuclei at the (K^-, K^+) reaction vertices on nuclei. If Ξ-nucleus bound states exist and their widths are small enough, we can see discrete peaks in K^+ momentum spectra which directly reflect the ΞN interaction. In addition to this clear signal, it is expected that double-hyperfragments produce after double-hyperon compound nuclear formation and evaporation process in the lower K^+ momentum region [4]. Actually, KEK-E176 [3] group have found $S = -2$ nuclei at the (K^-, K^+) reaction point in the emulsion target, although its mass cannot be specified. The (K^-, K^+) reaction also provides us with Ξ^- particles which can be used as a source of Ξ^- absorption at rest. Therefore, the study of the (K^-, K^+) reaction on nuclei is important and urgent to explore $S = -2$ nuclear systems. The relativistic heavy-ion collision is considered to be the third way to produce $S = -2$ nuclear systems. In this reaction, more strange nuclei ($S \leq -3$) or strangelets are expected to be produced. However, at the current stage, there is no positive report on the discovery of these nuclei, probably because the production cross section is too small to observe.

Recently, it has become experimentally possible to study double strangeness exchange reactions (K^-, K^+) on nuclear targets. For example, small angle (K^-, K^+) cross sections at $p_{K^-} = 1.65$ GeV/c were measured on several targets at KEK-PS by Iijima *et al.* [5]. The measured K^+ momentum spectrum shows a striking structure which gives rise to a target mass number dependence (A-dependence): In addition to quasifree peaks which correspond to elementary process of $K^-p \rightarrow K^+\Xi^-$, there appear a large bump spreading from $p_{K^+} = 0.35$ GeV/c to 1.0 GeV/c, and the yield of this bump in the lower momentum region grows much faster ($\sim A^{0.6}$) than that of the quasifree peak ($\sim A^{0.3}$) as the target mass increases. The comparison of the measured spectrum with the DWIA spectrum indicates that the high momentum peak $p_{K^+} \approx 1.1$ GeV/c has been understood by quasifree process $K^-p \rightarrow K^+\Xi$. However, the huge lower momentum bump cannot be explained by the quasifree processes only with well-known elementary reactions such as $K^-p \rightarrow K^+\Xi^*$ [5]. Thus, the appearance of this lower peak bump has casted a doubt on the belief that quasifree processes dominate

in meson induced reactions at around 1 GeV/c region, and at the same time, it gives us a hope that we can make more abundant double-hypernuclei from the unknown mechanism in this large bump. Therefore, it is important to obtain the knowledge for the reaction mechanism of the (K^-, K^+) reaction on nuclei.

Recently, one of possible mechanisms is proposed by Gobbi *et al.* [6]. They have claimed that a large part of the lower momentum peak is exhausted by the contribution from the heavy-meson production followed by its decay: $K^- p \to M\Lambda$, $M \to K^+ K^-$, where M is the $f_0(975)$, $a_0(980)$ or $\phi(1020)$ meson. It should be noted that the first reaction is a so-called subthreshold particle production. The treatment of the nucleon Fermi motion is considered to be important. Since the incident K^- particle has a large cross section with a nucleon in nuclear targets, the first-step reaction occurs mainly in the surface region where the Fermi momentum is smaller than that in the inner region. Although this reduction of the effective Fermi momentum should largely suppress the subthreshold particle production, it is not taken into account by Gobbi *et al.* In fact, we can see much less kaon pair creations $M \to K^+ K^-$ experimentally in the scintilator-fiber detector [7] than those expected in their calculations. Therefore, more detailed analyses of these reactions are desired before we conclude that the lower momentum bump comes from heavy-meson decays.

Another plausible process is the two-step strangeness exchange and production reaction, such as $K^- p \to M'Y$ followed by $M'N \to K^+ Y$, where M' and Y denote intermediate mesons $(\pi, \rho, \eta, \ldots)$ and hyperons $(\Lambda, \Sigma, \Lambda^*, \Sigma^*)$, respectively. In previous works [5, 6], the contributions of these two-step processes are estimated to be too small to explain the lower-momentum huge bump. However, these estimations limit the intermediate mesons and hyperons to pions and ground state hyperons, respectively. In addition, they considered only the ^{12}C target case. As pointed out by Iijima *et al.* [5], other possible reactions may contribute to the K^+ spectrum significantly. Furthermore, the target mass number dependence in the experimental spectrum is well-fitted with $A^{0.56 \pm 0.02}$ in the low momentum region, while $A^{0.38 \pm 0.03}$ in the high momentum region. This scaling property strongly suggests the contribution of multi-step processes [5]. Therefore, it is necessary to treat multi-step processes correctly to evaluate the K^+ momentum spectrum.

In this paper, we investigate multi-step effects in the (K^-, K^+) reactions on the various targets, i.e., ^{12}C, ^{27}Al, ^{63}Cu, ^{107}Ag and ^{208}Pb, using the intranuclear cascade (INC) model [10, 11, 12, 13]. One of our aims is to see the target mass number dependence on the K^+ momentum distribution in the (K^-, K^+) reaction. Thus as a first step, we neglect some other effects such as the influence of the potential effect between hadrons. We will also compare the results of the INC spectrum with the one-step process spectrum in the relativistic impulse approximation (RIA) model [46] to study the reaction (K^-, K^+) in detail.

In order to calculate the contributions of various two-step processes, there are two problems to be settled. The first problem is that they involve several elementary processes such as $\rho N \to KY$, whose cross sections cannot be measured experimentally. In this paper, we adopt the generalized Breit-Wigner formula [8, 9], in which s channel dominance is assumed and the interference effects between different baryon resonances

are ignored. It has been shown that this formula works well in the energy range under consideration, and it reduces theoretical ambiguities. The second problem lies in the treatment of complex multi-step processes. For the discussion of multi-step processes, cascade type models are considered to be the most reliable ones at the current stage: Each elementary two-body collision process is treated explicitly, then it is easy to include various multi-step processes. The INC model does quite well for many situations. After the first application to high-energy nuclear collisions [10, 11, 12, 13], it is also applied to pion-nucleus scattering [14, 15]. In these ten years, considerable efforts have been devoted to extend the INC model. One of them is the inclusion of mean-field effects within one-body theories [16, 17, 18, 19, 20, 22, 23, 24, 25] and N-body dynamics [26, 27, 28, 29, 30, 31, 32]. Furthermore, it becomes possible to describe the time-development of totally anti-symmetrized wave functions [33, 35]. These extended versions of the INC model are called microscopic transport models or microscopic simulations, and they have been successful in studying various aspects of heavy-ion collisions as well as light-ion induced reactions — particle production [36, 37, 21, 19], single-particle spectra [23], collective flow [16, 35], and fragment production [27, 30, 34, 38].

This paper is organized as follows: We describe our INC model in Sec. 2, and present a RIA model in Sec. 3. In Sec. 4, elementary cross sections are presented. In Sec. 5, we analyze the experimental data at KEK-E176 [5] and discuss the reaction mechanism of the (K^-, K^+) reactions. Finally, Section 6 contains our conclusion.

2　Intranuclear Cascade (INC) model

The Intranuclear cascade (INC) model we adopt here describes the propagation of the leading particle (the most energetic mesons at each time step). The momentum distribution of a nucleon in the target is assumed to be that of the Fermi gas, and the probability and the point of the collision between leading particle and the nucleon are determined by the mean free path of the propagating leading particle. This prescription is not fully microscopic, since the dynamical evolution of other particles is ignored. For example, we ignore the change of the nucleon momentum distribution and the secondary collision of a produced hyperon. However, this model is enough to describe the K^+ meson production, because other particles than the leading particle cannot produce the K^+ meson energetically and distortion of the target density is expected to be only important after the K^+ meson go out from the target.

Most of cascade type models are realized by the Monte-Calro procedure. There are several different prescriptions for a cascading of the colliding particles. One method is a so-called "closest distance approach" [12, 13]; if the minimum relative distance r_{min} for any pair of particles becomes less than $\sqrt{\sigma(\sqrt{s})/\pi}$, that pair is assumed to collide with each other, where $\sigma(\sqrt{s})$ is the total cross section for the pair at the c.m. energy $\sqrt{s}$. In another one, the collision frequency is determined by the mean free path. For example, the collision will take place with the probability $\sigma(\sqrt{s})v\rho(\mathbf{r})dt$ [10, 11, 15], where v and $\rho(\mathbf{r})$ are the relative velocity of the colliding pair and the nuclear density,

respectively. We have checked that the both methods give the same results for the K^+ momentum distribution in the (K^-, K^+) reaction However, other details may be different in several computer codes, therefore we explain our Monte-Calro procedure for completeness as follows:

1. The incoming K^- meson which is the first leading particle is boosted at the incident momentum $p_{K^-} = 1.65\text{GeV/c}$ in the laboratory frame.

2. To determine where this particle collides with a nucleon in the target nucleus ^AZ, we generate the Fermi momentum randomly with $p_F = (3\pi^2\rho_1)^{1/3}$, where $\rho_1 = \rho Z/A$, $\rho = Z/(4/3\pi R^2)$ and $R = 1.2A^{1/3}(\text{fm})$ in the case of matter distribution for the nucleus. If we employ the Fermi type nuclear density, the local Tomas-Fermi approximation is used to obtain the Fermi momentum $p_F(\mathbf{r})$.

3. The total cross section between the leading particle and the proton(neutron) $\sigma_\text{p}(\sigma_\text{n})$ is determined at this energy. If the leading particle is a resonance, the decay probability per unit length is calculated as $P_d = \Gamma/(v\gamma)$, where Γ is the total width of the resonance, v and γ denote the velocity and Lorentz gamma factor, respectively.

4. The mean free path is obtained as $\lambda = 1/(P_p + P_n + P_d)$, where $P_\text{p} = \sigma_\text{p}\rho_\text{p}$, $P_\text{n} = \sigma_\text{n}\rho_\text{n}$. We determine randomly the collision point according to the probability distribution $dP/\Delta r = \exp(-\Delta r/\lambda)/\lambda$: This distribution is realized by choosing Δr as follows.

$$\mathbf{r}' = \mathbf{r} + \Delta r\frac{\mathbf{p}}{|\mathbf{p}|} \tag{1}$$

with $\mathbf{p}$ is the momentum of the leading particle, where $\Delta r = -\lambda\log(1-x)$ and x is a random number between $0 \leq x < 1$.

5. If $|\mathbf{r}'|$ is larger than the nuclear radius R, cascading is regarded as finished. Otherwise, we select the branch randomly according to the probabilities of P_p, P_n and P_d.

6. If the leading particle is determined to collide with other nucleon, the collision branch is chosen randomly according to the partial cross sections, i.e. the elastic or inelastic collision between the leading particle and the nucleon. After choosing the branch, the kinematics of the collision is calculated, and the final momenta of particles after this collision are determined.

7. If particles after the collision are nucleons, the Pauli blocking is checked. If its momentum in the laboratory frame is smaller than the Fermi momentum 270 MeV/c, this collision is considered to be Pauli blocked and nothing occurs.

8. The procedures from 2 to 7 are repeated until this event finishes.

It is useful to mention here that our cascade procedure can be used only for the matter (constant) nuclear density $\rho = \rho_0\theta(R - |\mathbf{r}|)$. If more realistic density is used in

4

the calculations, as the Woods-Saxon type density, the collision prescription has to be modified. In that case, we change the collision rate according to Ref. [10, 15] or "closest distance approach". We have checked that the calculated K^+ momentum distribution does not depend on the cascading prescription.

Since the total cross sections are very small in the (K^-, K^+) reaction, note that a large amount of computational time is required to get sufficient statistics within the Monte Calro technique. In this work, therefore, while all the elastic scatterings and the relevant inelastic reactions described in Sec.4 are included, we ignore other non-interesting inelastic processes which do not result in the K^+ production; the probabilities for relevant inelastic reactions are increased by the factor of

$$F = \frac{\sigma_{tot} - \sigma_{el}}{\sum \sigma_k} \ , \tag{2}$$

where σ_k denotes the partial cross section for relevant inelastic reactions, and σ_{tot} and σ_{el} are the total and elastic cross sections at each collision energy, respectively. This procedure modifies the weight for each simulation, since we only treat the elastic scattering and relevant reactions. Thus when the relevant inelastic branch is chosen, the weight for the j-th simulation event after i-th step is defined as

$$w_i^j = w_{i-1}^j \frac{1}{F} \ , \tag{3}$$

where the initial value is $w_0^j = 1$. Under this assumption, the probability to detect the K^+ meson with a given impact parameter b is calculated as

$$\frac{d^2 P(b)}{dp d\Omega} = \frac{\sum_j w^j \Theta^j}{N_{ev}} \frac{1}{d\Omega_d dp} \tag{4}$$

with $d\Omega_d = 2\pi(\cos\theta_{min} - \cos\theta_{max})$, where $\theta_{min} = 1.7°$ and $\theta_{max} = 13.6°$ are the minimum and the maximum angles detected by the experimental measurement [5], respectively, and N_{ev} represents the number of events generated in the simulation. The weight w^j is defined as the final weight of the j-th event, and $\Theta^j = 1$ if the K^+ particle enters the detector range, otherwise $\Theta^j = 0$. Typically, we generate 1,000,000 events in this calculations.

In order to compare the theoretical results with the experimental data [5], we integrate the probability over the impact parameter $\mathbf{b}$:

$$\left\langle \frac{d^2\sigma}{dp d\Omega} \right\rangle^f = \int d\mathbf{b} \frac{d^2 P(b)}{dp d\Omega}, \tag{5}$$

where the definition of $\langle \rangle^f$ is the forward cross section averaged over the detected solid angle in the laboratory frame.

3   Relativistic impulse approximation (RIA) model

In this section, we explain the relativistic impulse approximation (RIA) [46] whose results are compared with those of INC. The RIA calculation in this paper is the

standard one in the quasifree region, and is essentially the same as Iijima *et al.* [5]. The one-step cross section $K^- + p \rightarrow K^+ + \Xi^-(\Xi^{*-})$ is calculated from the invariant matrix element $\mathcal{M}$ and the momentum distribution of a nucleon in the target nucleus:

$$d\sigma = Z_{eff}(K^-, K^+) \int \frac{d^3p_2 d\Gamma_3 d\Gamma_4}{4E_1 E_2 v_{12}} f(p_2) \langle |\mathcal{M}|^2 \rangle_S (2\pi\hbar)^4 \delta^4(p_1 + p_2 - p_3 - p_4) \quad (6)$$

$$d\Gamma_i = \frac{d^3p_i}{2E_i(2\pi\hbar)^3} , \quad f(p) = \left(\frac{4\pi P_F^3}{3}\right)^{-1} \theta(P_F - p) , \quad (7)$$

where the suffixes 1, 2, 3 and 4 represent K^-, p, K^+ and Ξ^-, respectively. As for the proton momentum distribution in nuclei $f(p_2)$, we have adopted Fermi gas model with $P_F = 0.27$ GeV/c. In this calculation, we use the parameterized elementary differential cross sections, as we will express in Sec. 4, so as to calculate the spin-averaged invariant matrix element squared $\langle |\mathcal{M}|^2 \rangle_S$ for elementary process of $K^- + p \rightarrow K^+ + \Xi^-/\Xi^{*-}(1530)$. The elementary cross section is written as

$$\frac{d\sigma^{elem.}(s)}{d\Omega_{CM}} = \frac{1}{4E_1 E_2 v_{12}} \frac{1}{(2\pi)^2} \frac{p_f}{4\sqrt{s}} \langle |\mathcal{M}|^2 \rangle_S , \quad (8)$$

where $\sqrt{s}$ and p_f are the invariant mass and the final c.m. momentum of the elementary process, respectively. Using Eqs. (6) (7) (8), we get the one-step quasifree cross sections as follows,

$$\frac{d^2\sigma}{dp_3 d\Omega_3} = Z_{eff}(K^-, K^+) \frac{p_3^2}{E_3} \int \frac{d^3p_2 d^3p_4}{E_4} f(p_2) \frac{\sqrt{s}}{p_f} \frac{d\sigma^{elem.}(s)}{d\Omega_{CM}} \delta^4(p_1 + p_2 - p_3 - p_4) . \quad (9)$$

In the RIA model, distortions of the initial K^- and final K^+ mesons are usually treated in the eikonal approximation. Thus the effective proton number $Z_{eff}(K^-, K^+)$ which represents the collision frequency of the particles, is given by

$$Z_{eff}(K^-, K^+) = \frac{Z}{A} \int d\mathbf{r} \rho(\mathbf{r}) \exp\left[-\sigma_{K^-} \int_{-\infty}^z \rho(x, y, z')dz' - \sigma_{K^+} \int_z^\infty \rho(x, y, z')dz'\right] , \quad (10)$$

where $\rho(\mathbf{r})$ denotes the nuclear density, and $\sigma_{K^-} = 29.0$mb and $\sigma_{K^+} = 18.4$mb are K^--nucleon and K^+-nucleon total cross sections, respectively.

For productions of the intermediate vector and scalar mesons and their decay, we use following expressions in RIA:

$$d\sigma = Z_{eff}(K^-, M) \int \frac{d^3p_2 d\Gamma_4}{4E_1 E_2 v_{12}} \frac{d\omega_3 d^3p_3}{(2\pi\hbar)^4} f(p_2) \langle |\mathcal{M}|^2 \rangle_S (2\pi\hbar)^4 \delta^4(p_1 + p_2 - p_3 - p_4)$$

$$\times d\Gamma_5 d\Gamma_6 (2\pi\hbar)^4 \delta^4(p_3 - p_5 - p_6) \quad (11)$$

$$\mathcal{M} = \mathcal{M}_{12 \rightarrow 34} G_3(\omega_3, \mathbf{p}_3) \mathcal{M}_{3 \rightarrow 56} \quad (12)$$

where the four momentum of the meson is represented as $p_3 = (\omega_3, \mathbf{p}_3)$, and the suffixes 1, 2, 3, 4, 5 and 6 represent K^-, p, M, Λ, K^+ and K^-, respectively. In this reaction, we have assumed that (1) the lifetime of the meson is long enough, and (2) the decay

6

occurs isotropically. The assumption (1) is realized by the approximation to the Green function G_3. In the case of the scalar meson, the Green function is given by

$$|G_3(\omega_3, \mathbf{p}_3)|^{-2} = \left|\omega_3^2 - E_3^2 + iM_3\Gamma_3\right|^2 \simeq \frac{2\pi}{4E_3 M_3 \Gamma_3} \delta(\omega_3 - E_3) , \qquad (13)$$

$$E_3 = \sqrt{M_3^2 + \mathbf{p}_3^2} , \qquad (14)$$

where Γ_3 is the total decay width of the meson. Note that the assumption (1) is already used in Eq.(11) implicitly, since the effective proton number $Z_{eff}(K^-, M)$ is calculated under the assumption that the meson M does not decay inside the nucleus. The matrix element $\mathcal{M}_{3\to 56}$ can be calculated under the assumption (2), which is obtained as

$$|\mathcal{M}_{3\to 56}|^2 = \frac{8\pi M_3^2 \Gamma_{3\to 56}}{p_f} , \quad p_f = \sqrt{M_3^2 - 4M_5^2}/2 . \qquad (15)$$

Thus, the differential cross section for the K^+ particle through the meson decay can be expressed as

$$E_{K^+}\frac{d^3\sigma}{dp_{K^+}^3} = \left(\frac{M_M}{M_K}\right)^2 Br(M \to K^+K^-) \int \frac{d\Omega_M}{4\pi} E_3 \frac{d^3\sigma(K^-A \to M\Lambda)}{dp_M^3} , \quad (16)$$

$$Br(M \to K^+K^-) = \Gamma_{M\to K^+K^-}/\Gamma_M , \qquad (17)$$

where the solid angle Ω_M is calculated in the rest frame of K^+, and $E_3 d^3\sigma(K^-A \to M\Lambda)/dp_M^3$ denotes the invariant cross section for the one-step intermediate meson production per a proton, which is given by Eq.(9) without the effective proton number Z_{eff}.

4   Elementary cross sections

Now let us explain the elementary cross sections used in this paper. All the energies and cross sections are give in GeV and mb unit, respectively. We have categorized the events into three types. The first category is the direct-type reaction, which concerns the one-step double strangeness exchange reaction ($\bar{K}N \to K\Xi, K\Xi^*$). The second one is the heavy scalar and vector meson productions and their decay ($\bar{K}N \to MY, M \to K^-K^+$) proposed by Gobbi $et\ al.$ [6]. The third type is the two-step strangeness exchange and production reaction, such as $\bar{K}N \to \pi Y$ followed by $\pi N \to KY$. We will explain the necessary elementary cross sections in this order.

The following processes are necessary to describe the direct-type double strangeness exchange reaction.

(A) All the elastic scatterings and charge exchange reactions of KN and $\bar{K}N$.

(B) Double strangeness exchange processes:

$\bar{K}N \to K\Xi,\ K\Xi^*(1530).$

(C) Initial anti-kaon interaction:

$$\bar{K}N \rightarrow \bar{K}^*(892)N.$$

(D) Decay of resonance kaons (anti-kaons):

$$K^*(892) \rightarrow K\pi, \ \bar{K}^*(892) \rightarrow \bar{K}\pi,$$

(E) Final kaon interactions:

$$KN \rightarrow (K^*(892)N, \ K\Delta(1232)),$$
$$K^*(892)N \rightarrow (KN, \ K^*(892)\Delta(1232)).$$

Although the actual strangeness exchange occurs only in the processes of (B), initial and final state interactions have to be included when we are interested in the absolute and whole spectrum of K^+ including the lower momentum region, as will be demonstrated in Sec. 5.

The above cross sections are fitted to the experimental data [39, 40] with appropriate functions or tabulated. The total, elastic and charge exchange cross sections of (A) are well-known experimentally [39, 41]. We employ here the smooth interpolations of these data. Angular dependencies of the elastic collisions are simply assumed to have the form [12, 16]

$$\frac{d\sigma}{dt} \propto \exp(b(\sqrt{s})t) , \tag{18}$$

where t denotes the square of the transferred four momentum, $\sqrt{s}$ is the c.m. energy, and $b(\sqrt{s})$ is taken to be $b(\sqrt{s}) = 0.125\sigma(\sqrt{s})_{tot}$.

The double strangeness exchange reactions (B) are also well-known experimentally although the errorbars are still large. Therefore, we use following parameterization for the elementary Ξ and $\Xi^*(1530)$ production cross sections:

$$\sigma(K^-p \rightarrow K^+\Xi^-) = \begin{cases} \dfrac{0.0413463(\sqrt{s} - 1.81496)^{1.68792}}{(\sqrt{s} - 1.93536)^2 + 0.01174} \quad [\text{mb}] \qquad \sqrt{s} \leq 2.22[\text{GeV}/c] \\[2mm] \dfrac{0.00613(\sqrt{s} - 1.81496)^{0.48020}}{(\sqrt{s} - 2.02435)^2 + 0.01739} \\[2mm] \quad + \dfrac{0.001673(\sqrt{s} - 2.11496)^{0.338065}}{(\sqrt{s} - 2.3174)^2 + 0.016429} \quad [\text{mb}] \qquad \sqrt{s} > 2.22[\text{GeV}/c] \end{cases}$$

$$\tag{19}$$

$$\sigma(K^-p \rightarrow K^0\Xi^0) = \frac{0.00364308(\sqrt{s} - 1.812571)^{0.620511}}{(\sqrt{s} - 2.05469)^2 + 0.0184015} \quad [\text{mb}] , \tag{20}$$

$$\sigma(K^-p \rightarrow K^+\Xi^{*-}(1530)) = \frac{0.0017692(\sqrt{s} - 2.0264)^{0.45434}}{(\sqrt{s} - 2.09274)^2 + 0.01394} \quad [\text{mb}] , \tag{21}$$

$$\sigma(K^-p \rightarrow K^0\Xi^{*0}(1530)) = \frac{0.003854(\sqrt{s} - 2.0264)^{0.3475}}{(\sqrt{s} - 2.18855)^2 + 0.028487} \quad [\text{mb}] . \tag{22}$$

These fitted cross sections are shown in Fig. 1, together with the experimental data. Although we can take another parameterizations within the experimental error bars, we have checked that our simulation results are almost the same.

Around the incident momentum of $p_{K^-} = 1.65$ GeV/c for the K^- beam, the experimental data shows a backward peak angular distribution. We fit angular distributions of Ξ production cross sections to the experimental data at $p_{K^-} = 1.7$ GeV/c, neglecting these energy dependence:

$$\frac{d\sigma}{d\Omega} \sim \begin{cases} 0.34308 \exp(0.6229\cos\theta) + 0.06681 \exp(-4.4396\cos\theta) & \text{for } K^-p \to K^+\Xi^- \,, \\ 0.44 \exp(3.1684\cos\theta) + 0.5428 \exp(-1.6747\cos\theta) & \text{for } K^-p \to K^0\Xi^0 \,. \end{cases} \tag{23}$$

As shown in Fig. 2, this parameterization is a good approximation within a Fermi momentum spreading around $p_{K^-} = 1.65$ GeV/c. For the $\Xi^*(1350)$ production, the angular distributions are assumed to be isotropic.

In order to describe the reactions in the second category, following elementary cross sections and the decay widths are required.

(F) Scalar and vector meson production:

$$\bar{K}N \to (\phi, a_0, f_0)\Lambda.$$

(G) Decay of scalar and vector mesons:

$$(\phi, a_0, f_0) \to K^-K^+.$$

Compared to the processes of (A)–(E), the experimental information on the scalar and vector meson ($\phi/f_0/a_0$) production is very scarce. Here, $\phi/f_0/a_0$ production cross sections and angular distributions are taken from Ref. [6]:

$$\sigma(K^-p \to \phi + \Lambda) = 0.31531p_f \exp(-1.45p_f) \quad [\text{mb}], \tag{24}$$

$$\sigma(K^-p \to f_0 + \Lambda) = 1.51\sigma(K^-p \to \phi + \Lambda), \tag{25}$$

$$\sigma(K^-p \to a_0 + \Lambda) = 1.38\sigma(K^-p \to \phi + \Lambda), \tag{26}$$

$$\frac{d\sigma}{d\Omega} \sim \exp\left(1.8\cos\theta\right), \tag{27}$$

where p_f is the relative momentum for the final state. The angular distribution of the ϕ decay into $\bar{K}K$ is assumed to be isotropic in its rest frame. But we have checked that an anisotropic decay ($\cos^2\theta$ distribution) has no significant influence in our results.

For two-step processes, in the case of the ^{12}C target, Iijima *et al.* [5] found that the calculated cross section is smaller than the observed one in an order of magnitude. Moreover, Gobbi *et al.* [6] also suggested that two-step processes can not reproduce the experimental cross section at low momentum region in the K^+ spectrum. Note, however, that the intermediate meson is limited to the pion, and they considered only for the ^{12}C target case. We expect that inclusion of heavy mesons as η mesons would strongly affect the final results especially in the case of heavier nucleus. Therefore, we take account of two-step processes on all targets by including following processes:

9

(H) Single strangeness exchange reactions:

$$\bar{K}N \to (\pi, \rho, \eta, \omega, \eta')(Y, Y^*) \ .$$

(I) Single strangeness creation reactions:

$$(\pi, \rho, \eta, \omega, \eta')N \to (K, K^*)(Y, Y^*), \ \phi N \ .$$

(J) Decay of resonances:

$$\rho \to 2\pi, \ \omega \to 3\pi.$$

Here, $Y = \{\Lambda, \Sigma\}$, $Y^* = \{\Lambda(1405), \Lambda(1520), \Sigma(1385)\}$ and $K^* = \{K^*(892)\}$. We treat explicitly the isospin of all these particles in our calculations.

We have fitted the experimental data as far as they are available. The fitted function is partly taken from Refs. [50, 52] (see Appendix). Other unknown cross sections in the second step (I), are estimated using the Breit-Wigner formula in the same way as Ref. [8, 9]. Namely, processes of (I) are assumed to occur through N^*, Δ^* resonances and interferences of various resonances are ignored. Since the energy is located just at the baryonic resonance region in the (K^-, K^+) reaction with the incident momentum of $p_{K^-} = 1.65$ GeV/c, this assumption is expected to be valid. The explicit form is expressed as

$$\sigma(MB \to M'B') = \frac{\pi}{k_{cm}^2} \sum_R \frac{(2J_R + 1)}{(2S_M + 1)(2S_B + 1)} \frac{\Gamma_R(MB)\Gamma_R(M'B')}{(\sqrt{s} - m_R)^2 + \Gamma_R(tot)^2/4} \quad (28)$$

with the momentum dependent width

$$\Gamma_R(MB) = \left(\frac{p}{p_R}\right)^{(2\ell+1)} \frac{1.2 m_R/\sqrt{s}}{1 + 0.2(p/p_R)^{2\ell}} \Gamma_R^0(MB) \ , \quad (29)$$

where $\Gamma_R^0(MB)$ denotes the partial width of the $R \to MB$ decay, and

$$p = \frac{\sqrt{(\sqrt{s} - (m_B + m_M))(\sqrt{s} - (m_B - m_M))}}{2\sqrt{s}} \ , \quad (30)$$

$$p_R = \frac{\sqrt{(m_R - (m_B + m_M))(m_R - (m_B - m_M))}}{2\sqrt{s}} \ , \quad (31)$$

are the relative momenta between the meson and the baryon in the final state at a given c.m. energy and the resonance mass, respectively. The summation R in Eq.(28) runs over resonances, as $N(1440) \sim N(2190), \Delta(1600) \sim \Delta(1950)$. This formula is called as the generalized Breit-Wigner formula, which is obtained by neglecting t channel contributions and the interference of the resonances. Actual values for these parameters are taken from the Particle Data Group [41], as listed in Tables 1 and 2.

$$\underline{\text{Table. 1}}$$

Table. 2

The formula Eq. (28) enables us to estimate experimentally inaccessible cross sections such as $\rho N \to \Lambda K$. The N^* resonances decaying into the ωN and $\eta' N$ branches are included to fit the experimental data of $\pi^- p \to \omega n(\eta' n)$ [39]. It has been shown that such meson resonances play an important role to product strangeness particles in heavy-ion collisions at AGS and SPS energies [9]. In fact, strangeness production cross sections via the meson resonances are found to be much larger than πN cross sections.

Although t channel component of $\bar{K} N$ interactions are considered to be large in (H), we also apply the resonance formula of Eq.(28) taking into account hyperon resonances $\Lambda(1520) \sim \Lambda(2350)$ and $\Sigma(1660) \sim \Sigma(2250)$ in order to obtain the cross sections. However, there is a lack of experimental information about resonance parameters compared with N^* and Δ^*. Therefore, we determined the experimentally unknown resonance parameters to fit the existing data [40] such as $K^- p \to \eta \Lambda$. The parameters are shown in Tables 3 and 4. This procedure would be sufficient for this study because we need only $\bar{K} N$ interaction cross sections as the incoming states. If we cannot obtain the cross sections and angular dependencies from the Breit-Wigner formula or from the experimental data, for example, $\sigma(\rho^- p \to \Sigma^0 K^0(892))$, we simply assume that these values are the same as πN cross sections at the same c.m. energies. For the total cross section of ϕN, we have used the value of 8.3mb, which was suggested in a photoproduction experiment [43], while 16.0mb is predicted in the additive-quark model Ref. [9].

Table. 3

Table. 4

Note that the process $\phi N \to K \Lambda$ is also able to produce the K^+ meson. The cross section calculated from the OBE model of Ref. [44] amounts to about 5mb, as seen in Fig. 3. Our INC calculation includes this process as a two-step process.

Fig. 3

5   Results and Discussions

5.1 Ξ and $\Xi^*(1535)$ Productions

Let us now compare our results with the experimental data. At first, we focus on the Ξ and $\Xi^*(1535)$ production processes. In Fig. 4, we display the INC spectra using both the matter density (solid lines) and the Fermi-type nuclear density (dashed lines) for (K^-, K^+) reactions on ^{12}C, ^{27}Al, ^{63}Cu, ^{107}Ag and ^{208}Pb targets. The RIA results with matter density are also presented (dotted lines).

Fig. 4

We can see that the results with the Fermi-type density well reproduce the experimental data at the high momentum region, while the results with the matter density underestimate the experimental data. Our calculations with Fermi-type nuclear density for Ξ and Ξ^* production processes are consistent with DWIA of Ref. [5], which was calculated by using the same nuclear density [45]. It is also seen that the INC and the RIA results with matter density give almost the same results around the high momentum region of K^+, including the shape and absolute value of the spectrum. The difference can be found in the lower momentum region of K^+. This is due to the different treatment of initial and final state interactions. The eikonal approximation of Eq. (10) means that once the particle is scattered, the flux is assumed to be lost in the RIA model. On the other side, the INC model treats the initial and final state interactions explicitly, which ensure us that both loss and gain of the flux are automatically included. For example, some parts of the scattered K^+ particles will be detected while the momentum becomes lower than that just after the production.

5.2 Contributions of the scalar and vector meson decays

Here we consider the effect through the scalar(a_0/f_0) and the vector meson(ϕ) decays. The importance of this process were first suggested by Gobbi *et al.* [6]. In Fig. 5, we present the calculated results of the K^+ spectra (solid lines), taking into account the decay from ϕ, a_0 and f_0 mesons; the $\phi/f_0/a_0$ production and their decay into K^-K^+ significantly contribute to the K^+ spectrum at low momentum region. However, these processes are not enough to reproduce the large bump in the experimental data.

Fig. 5

In order to test these results, we also calculate the cross section of the above processes employing RIA. The RIA results are shown in Fig. 5 (dotted lines). We find that INC and RIA calculations give us similar results for all targets. However, our results are about 50% smaller than the cross section in Ref. [6]. There are several probable reasons for this contradiction. The one reason lies in the treatment of the Fermi motion in nuclei. Since the $\phi/f_0/a_0$ mesons can be produced by a subthreshold particle production in the (K^-, K^+) reaction at $p_{K^-} = 1.65$ GeV/c, the effect of the Fermi motion is expected to be very important in this situations [47, 21]. Thus we have checked the sensitivity of the treatment for the Fermi motion. As seen in Fig. 6, we compare the results of following calculations for the ^{27}Al target with the matter density (matter), the local Fermi momentum with the Fermi type nuclear density (F+F) and the matter Fermi momentum with the Fermi type nuclear density (F+M). It can be seen that the cross section in case (F+M) is enhanced by the factor 1.3. This treatment corresponds to the calculation in Ref. [6].

Fig. 6

In addition, we mention that Gobbi et al. [6] used an "effective" incident momentum which includes the effects of nucleon Fermi motion, and regarded it as the incident momentum. If this effective incident momentum is used in the original laboratory frame, it gives a wrong kinematics. In fact, the high momentum threshold of the K^+ particle is artificially modified to be about 1.1 GeV/c in Ref. [6], while the actual threshold is about 0.8 GeV/c through $\phi/a_0/f_0$ decays.

5.3 Two-Step Processes

In Figs. 7 and 8, we show the calculated K^+ spectra through two-step processes (dotted lines) on ^{12}C, ^{27}Al, ^{63}Cu, ^{107}Ag and ^{208}Pb targets: Long dashed lines denote the contributions of the Ξ and Ξ^* production, dashed lines represent those from $\phi/a_0/f_0$ decay, and solid lines are the sum of all the processes considered in this paper. It is clearly observed that two-step processes play an significant role in K^+ yields, especially for heavier targets. This result is in contrast to Ref. [5, 6]. In addition, the calculated total spectra well reproduce the experimental data.

$$\boxed{\text{Fig. 7}}$$

$$\boxed{\text{Fig. 8}}$$

Before concluding that two-step processes are important, we should estimate theoretical ambiguities in the present calculation. We consider that the largest ambiguities come from the angular distributions of elementary processes. Here we have used the experimental angular distributions if possible, for example, the Ξ, Ξ^*, ϕ productions and some part of two-step processes. The experimentally unknown angular distributions of two-step processes such as ρN are simply assumed to be the same dependence to that of πN at same c.m.energy. Therefore, it is necessary to estimate the sensitivity of the angular distributions. In Fig. 9, we represent the results of the two-step contributions assuming the isotropic angular distribution for all of the two-step reactions. This choice decreases forward angle cross sections, but the difference of integrated yields is at most 30%, and their contributions are still significant. Due to the large uncertainty of the elementary angular distribution like $\rho N \rightarrow KY$, more quantitative discussions are impossible at this stage. However, we can conclude that a significant part of K^+ particles are produced though various two-step processes, since the use of isotropic angular distribution might give the minimum yields of K^+.

$$\boxed{\text{Fig. 9}}$$

Contrast to the previous works [5, 6], the reasons why two-step processes have large cross sections can be understood as follows. The first reason is that we take account of the meson resonances ρ, η, ω as a intermediate meson. In addition to the increase of the number of processes resulting in K^+ production, due to the large masses of meson resonances, the strangeness productions through these mesons have a larger

cross section than that through pions. Note that the πN reaction for strangeness productions is all endoergic one ($Q < 0$), whereas ρ-, η- and ω-nucleon reactions for strangeness productions are exoergic one ($Q > 0$). Thus inclusion of these mesons is of importance. Figure 10 displays the contributions of intermediate mesons. It can be seen that π, η and ω mesons mainly contribute to the two-step cross sections. It is of importance to see that the cross sections of meson resonances are comparable to that of pions. The reason of the small ρ-contribution is that the ρ meson are likely to decay before its collision due to its large width. We find also that pions from the ρ meson decay can contribute to yields of K^+. We confirm that if we include only pions as the intermediate meson and neglect hyperon resonances, this calculation gives similar result to the estimation of Iijima *et al.* in the case of ^{12}C target: As expected from the small mass number, the contribution from the two-step processes is rather smaller than that for the heavier targets.

$$\boxed{\text{Fig. 10}}$$

The second reason is related to the meson momentum region. The mesons produced by K^- at $p_{K^-} = 1.65\text{GeV/c}$ are just in the baryon resonance region where the cross sections have the largest values. Alternatively, at the higher momentum of K^-, the contribution of the ϕ meson and its decay becomes larger, and K^+ from the ϕ meson decay would dominate K^+ yields.

We can also consider the $\phi N \to K^+\Lambda$ process. Using the OBE model [44], we can obtain the cross section about 5mb at most. Although this process is taken into account in the INC calculation, it is found that the contribution is small.

6   Summary and Conclusions

In this paper, we have analyzed (K^-, K^+) reactions within a INC model that is newly developed especially to include various inelastic channels in order to investigate the whole momentum region of the K^+ momentum. The detailed comparison for the K^+ spectrum has been done between the INC and the RIA model calculations. We have shown that the results with these two models reasonably agree with each other in one-step processes, and the calculated total spectra with INC well reproduce the experimental data on various targets.

Our results show that the momentum distribution of K^+ can be explained mainly by following mechanisms:

(1) Direct-type reactions:

$$K^-p \to K^+\Xi^- \;,$$
$$K^-p \to K^+\Xi^{*-}(1530) \;.$$

(2) Decay of scalar/vector mesons:

$$K^- p \rightarrow \left\{ \begin{array}{c} \phi \\ a_0 \\ f_0 \end{array} \right\} \Lambda, \quad \left\{ \begin{array}{c} \phi \\ a_0 \\ f_0 \end{array} \right\} \rightarrow K^- K^+.$$

(3) Two-step processes:

$$K^- N \rightarrow \left\{ \begin{array}{c} Y \\ Y^* \end{array} \right\} M, \quad \text{followed by} \quad MN \rightarrow \left\{ \begin{array}{c} K \\ K^* \end{array} \right\} \left\{ \begin{array}{c} Y \\ Y^* \end{array} \right\},$$
where $M = \pi, \rho, \eta, \omega$.

For the process (1) and the process (2), the consistent results are obtained between the INC and the RIA models. Among two-step processes (3), it is important to include π, ρ, η, ω mesons, and hyperon and kaon resonances to reproduce the K^+ spectrum. There are mainly two reasons of the enhancement of the two-step contributions, contrary to the estimation in the previous works [5, 6]. The first one is the variety of intermediate mesons and final hyperons. It is clear that a number of the path resulting in K^+ production is much larger, because various mesons and hyperon resonances are included. In addition, meson resonances have larger masses than pions, and stored energies in masses are released in second step reactions. Thus the K^+ production cross section with these meson resonances becomes larger than that of pions. The second reason is related to the meson momentum region. The mesons produced in this reaction is just in the baryon resonance region where the cross sections have the largest values.

In conclusion, the INC model can explain consistently the K^+ momentum spectrum from the (K^-, K^+) reaction at $p_{K^-} = 1.65 \text{GeV/c}$ on various targets. Both the two-step strangeness exchange and production processes with various intermediate mesons and ϕ, a_0 and f_0 productions and their decay into $K^+ K^-$ of which was first quoted in Ref. [6], are necessary to reproduce the experimental data in the low momentum region.

There are still some theoretical ambiguities and problems in the present study. One of them is, as already discussed in Sec. 5, the angular distribution of elementary processes. Another problem is that we have ignored the propagation of heavy baryon resonances which are assumed to be formed in Eq. (28); however, the lifetimes of these heavy resonances are so small that they are expected to decay before interacting with other nucleons at around the normal nuclear density. The third one is the branching ratios of heavy baryon resonances, especially decaying into ωN. Since the measurement of decaying into ωN is relatively difficult, the experimental information of the branching ratio is scarce. Although we have fitted the ω production cross sections and determined the plausible branching ratios, it may be problematic to assume this reaction occurs only in s channel. These facts may be related to the overestimation of the K^+ spectra at very low momentum region.

There are some interesting problems suggested in this work. First, we note that the (K^-, K^+) reaction can produce hyperon resonances Y^* in the nuclear medium. This opens up the possibility of studying the properties of the hyperon resonances in nuclear matter. Another interesting problem is to predict yields of double-Λ hyperfragment

production and to make their production mechanism clear. This is possible if we extend our cascade code including mean field effects [26, 27, 28, 29, 30, 31, 32]. In order to search for double-Λ hypernucleus experimentally, the (K^-, K^+) experiment is planned at AGS(E906) [48, 49] in the near future. The production mechanism of hyperfragments may be different from the K^+ productions through direct Ξ, direct Ξ^*, ϕ decay and two-step processes. The study in this line is now in progress.

Acknowledgement

A Parameterizations of Cross Sections and Angular Distributions

A.1 Cross Sections

We list up the cross sections parametrzied with the experimental data. Some parameterizations are taken from Ref. [50, 51, 52].

$$\sigma(K^-p \to \Lambda\eta') = \frac{0.02(\sqrt{s} - \sqrt{s_0})^{0.4}}{(\sqrt{s} - 2.20726)^2 + 0.0589288} + \frac{0.000186093(\sqrt{s} - \sqrt{s_0})}{(\sqrt{s} - 3.07199)^2 + 0.00652879} \quad (32)$$

$$\sigma(\pi^-p \to \Lambda K^0) = \frac{0.007665(\sqrt{s} - 1.613)^{0.1341}}{(\sqrt{s} - 1.72)^2 + 0.007826} \quad (33)$$

$$\sigma(\pi^-p \to \Sigma^-K^+) = \frac{0.009803(\sqrt{s} - 1.688)^{0.6021}}{0.006583 + (\sqrt{s} - 1.742)^2} + \frac{0.006521(\sqrt{s} - 1.688)^{1.4728}}{0.006248 + (\sqrt{s} - 1.940)^2} \quad (34)$$

$$\sigma(\pi^-p \to \Sigma^0K^0) = \frac{0.05014(\sqrt{s} - 1.688)^{1.2878}}{0.006455 + (\sqrt{s} - 1.730)^2} \quad (35)$$

$$\sigma(\pi^-p \to \Lambda(1405)K^0) = \frac{0.02655(\sqrt{s} - 2.018)^{0.5378}}{(\sqrt{s} - 2.0754)^2 + 0.1808} \quad (36)$$

$$\sigma(\pi^-p \to \Lambda(1520)K^0) = \frac{0.00963763(\sqrt{s} - 1.833)^{1.68811}}{(\sqrt{s} - 2.21759)^2 + 0.0249613} \quad (37)$$

$$\sigma(\pi^-p \to \Lambda K^0(892)) = 0.240985q\exp(-1.09397q), \quad (38)$$

$$\text{where } q = \frac{\sqrt{(s - (M_\Lambda + 0.636))(s - (M_\Lambda - 0.636))}}{2\sqrt{s}} \quad (39)$$

16

$$\sigma(\pi^- p \to \Sigma^-(1385)K^+) = \frac{0.00163105(\sqrt{s} - 1.752)}{(\sqrt{s} - 2.1833)^2 + 0.0114982} \tag{40}$$

$$\sigma(\pi^- p \to \Sigma^0(1385)K^0) = \frac{0.0113016(\sqrt{s} - 1.752)}{(\sqrt{s} - 2.12476)^2 + 0.0636864} \tag{41}$$

$$\sigma(\pi^- p \to \Sigma^- K^+(892)) = 0.123117q \exp(-1.50466q), \tag{42}$$

$$\text{where } q = \frac{\sqrt{(s - (M_{\Sigma^-} + 0.636))(s - (M_{\Sigma^-} - 0.636))}}{2\sqrt{s}} \tag{43}$$

$$\sigma(\pi^- p \to \Sigma^0 K^0(892)) = 0.188256q \exp(-1.32449q), \tag{44}$$

$$\text{where } q = \frac{\sqrt{(s - (M_{\Sigma^0} + 0.636))(s - (M_{\Sigma^0} - 0.636))}}{2\sqrt{s}} \tag{45}$$

$$\sigma(\pi^- p \to n\phi) = \frac{0.000986473(\sqrt{s} - 1.948)^{0.045244}}{(\sqrt{s} - 2.09)^2 + 0.0290906} \tag{46}$$

$$\sigma(\pi^+ p \to \Sigma^+ K^+) = \frac{0.03591(\sqrt{s} - 1.688)^{0.9541}}{0.01548 + (\sqrt{s} - 1.890)^2} + \frac{0.1594(\sqrt{s} - 1.688)^{0.01056}}{0.9412 + (\sqrt{s} - 3.000)^2} \tag{47}$$

$$\sigma(\pi^+ p \to \Sigma^+(1385)K^+) = \frac{0.0191992(\sqrt{s} - 1.833)^{0.983665}}{(\sqrt{s} - 1.98968)^2 + 0.0253142} \tag{48}$$

$$\sigma(\pi^+ p \to \Sigma^+ K^+(892)) = \frac{0.0361293(\sqrt{s} - 1.829)^{0.1}}{(\sqrt{s} - 2.37123)^2 + 0.177898} \tag{49}$$

$$\sigma(\pi^0 p \to \Sigma^0 K^+) = \frac{0.003978(\sqrt{s} - 1.688)^{0.5848}}{0.006670 + (\sqrt{s} - 1.740)^2} + \frac{0.04709(\sqrt{s} - 1.688)^{2.1650}}{0.006358 + (\sqrt{s} - 1.905)^2} \tag{50}$$

$$\sigma(\pi^0 p \to \Sigma^+ K^0) = \frac{0.05014(\sqrt{s} - 1.688)^{1.2878}}{0.006455 + (\sqrt{s} - 1.730)^2} \tag{51}$$

A.2 πN Angular Distributions

The angular distributions are fitted as the following function,

$$\frac{d\sigma}{d\Omega} \sim a \exp(\gamma_1 \cos\theta) + b \exp(-\gamma_2 \cos\theta) + c(1 - \cos^2\theta) \tag{52}$$

at the c.m. energy s in GeV.

1. $\pi^- p \to \Lambda K^0$

$$c = 0, \tag{53}$$

$$a = \begin{cases} -5616.87 + 6491.43s - 1859.92s^2, & s \le 1.878, \\ \dfrac{0.0962773}{(s - 1.89039)^2 + 0.00650021}, & s > 1.878, \end{cases} \tag{54}$$

$$b = \begin{cases} 0.0 & s < 1.878, \\ -155.986 + 240.621s - 123.717s^2 + 21.2028s^3, & 1.878 \le s < 2.024, \\ -4.72881 + s^{2.20857}, & 2.024 \le s < 2.097, \\ -65.8086 + 64.8666s - 15.8761s^2, & 2.097 \le s < 2.35, \\ 0.0, & s \ge 2.35, \end{cases}$$

$$\gamma_1 = \begin{cases} -9.54489 + 6.20974s, & s < 1.878, \\ 28.4659 - 33.8566s + 10.3904s^2, & s \geq 1.878, \end{cases} \tag{55}$$

$$\gamma_2 = 83.5865 - 55.3861s + 8.68325s^2. \tag{56}$$

2. $\pi^- p \rightarrow \Sigma^- K^+$

$$c = 0.0 \tag{57}$$

$$a = \begin{cases} 0.0049, & s < 1.978, \\ 0.0, & s \geq 1.978, \end{cases} \tag{58}$$

$$b = \begin{cases} 0.3632, & s < 1.978, \\ 1.0, & s \geq 1.978, \end{cases} \tag{59}$$

$$\gamma_1 = 4.32675, \tag{60}$$

$$\gamma_2 = \begin{cases} 1.38911, & s < 1.978, \\ 378.699 - 361.502s + 86.4954s^2, & 1.978 \leq s < 2.097, \\ -8.44056 + 4.53549s & s \geq 2.097. \end{cases} \tag{61}$$

$$\tag{62}$$

3. $\pi^- p \rightarrow \Sigma^0 K^0$

$$c = 0.0, \tag{63}$$

$$a = 0.00537342, \tag{64}$$

$$b = 0.391835, \tag{65}$$

$$\gamma_1 = 5.17482, \tag{66}$$

$$\gamma_2 = 0.582968. \tag{67}$$

4. $\pi^+ p \rightarrow \Sigma^+ K^+$

$$a = \begin{cases} 0.00806605, & s < 1.9, \\ 0.000323596, & s \geq 1.9, \end{cases} \tag{68}$$

$$b = \begin{cases} 10.0601, & s < 1.9, \\ 0.00018645, & s \geq 1.9, \end{cases} \tag{69}$$

$$c = \begin{cases} 0.0, & s < 1.9 \\ 38.3724 & s \geq 1.9, \end{cases} \tag{70}$$

$$\gamma_1 = \begin{cases} 7.49409, & s < 1.9, \\ 13.3355, & s \geq 1.9, \end{cases} \tag{71}$$

$$\gamma_2 = \begin{cases} 0.889499, & s < 1.9, \\ 13.3355. & s \geq 1.9. \end{cases} \tag{72}$$

$$\tag{73}$$

References

[1] C. B. Dover and G. E. Walker, Phys. Rep. **89** (1982) 1.

[2] M. Danyz *et al.*, Nuc. Phys. **49** (1963) 121; D. J. Prowse, Phys. Rev. Lett. **17** (1966) 782; S. Aoki *et al.*, Prog. Theor. Phys. **85** (1991) 1287.

[3] S. Aoki *et al.*, preprint (1995).

[4] M. Sano, M. Wakai and Y. Yamamoto, Prog. Theor. Phys. **87** (1992) 957.

[5] T. Iijima *et al.*, Nuc. Phys. **A546** (1992) 588.

[6] C. Gobbi, C. B. Dover and A. Gal, Phys. Rev. **C50** (1994) 1594.

[7] K. Imai, private communication.

[8] G. E. Brown, C. M. Ko, Z. G. Wu and L. H. Xia, Phys. Rev. **C43** (1991) 1881.

[9] H. Sorge *et al.*, Phys. Lett. **B271** (1991) 37; H. Sorge *et al.*, Z. Phys. **C59** (1993) 85.

[10] K. Chen, Z. Frankel, G. Friedlander, J. R. Grover, J. M. Miller and Y. Shimamoto, Phys. Rev. **166** (1968) 949.

[11] Y. Yariv and Z. Frankel, Phys. Rev. **C20**, 2227 (1979).

[12] J. Cugnon, Phys. Rev. **C22** (1980) 1885; J. Cugnon, T. Mizutani and J. Vandermeulen, Nucl. Phys. **A352** (1981) 505.

[13] J. Cugnon, D. Kinet and J. Vandermeulen, Nucl. Phys. **A379** (1982) 553; J. Cugnon, Nucl. Phys. **A387** (1982) 191c.

[14] J. N. Ginocchio, Phys. Rev. **C17** (1978) 195; J. N. Ginocchio and M. B. Johnson, Phys. Rev. **C21** (1980) 1056; Z. Frankel, E. Piasetzky and G. Kalbermann, Phys. Rev. **C26**, (1982) 1618.

[15] L. L. Salcedo, E. Oset, M. J. Vicente-Vacas and C. Garcia-Recio, Nucl. Phys. **A484** (1988) 557; M. J. Vicente-Vacas and E. Oset, Nucl. Phys. **A568** (1994) 557.

[16] G. F. Bertsch and S. Das Gupta, Phys. Rep. **160** (1988) 189.

[17] G. F. Bertsch, H. Kruse and S. Das Gupta, Phys. Rev. **C29** (1984) 673.

[18] J. Aichelin and G. F. Bertsch, Phys. Rev. **C31** (1985) 1730.

[19] W. Cassing, V. Metag, U. Mosel and K. Niita, Phys. Rep. **188** (1990) 363.

[20] W. Cassing and U. Mosel, Prog. Part. Nucl. Phys. **25** (1990) 235.

[21] U. Mosel, Annu. Rev. Nucl. Part. Sci. **41** (1991) 29.

[22] H. Söcker and W. Greiner, Phys. Rep. **137** (1986) 277.

19

[23] H. Kruse, B. V. Jacak and H. Stöcker, Phys. Rev. Lett. **54** (1985) 289.

[24] J. J. Molitoris and H. Stöcker, Phys. Rev. **C32** (1985) 346; Phys. Lett. **B162** (1985) 47.

[25] J. J. Molitoris, H. Stöcker and B. L. Winer, Phys. Rev. **C36** (1987) 220.

[26] J. Aichelin, Phys. Rep. **202** (1991) 233.

[27] G. Peilert, J. Konopka, H. Stöcker and W. Greiner, Phys. Rev. **C46** (1992) 1457

[28] M. Berenguer, C. Hartnack, G. Peilert, H. Stöcker, W. Greiner, J. Aichelin and A. Rosenhauer, J. Phys. **G18** (1992) 655.

[29] A. Bohnet, N. Ohtska, J. Aichelin, R. Linden and A. Faessler, Nucl. Phys. **A494** (1989) 349.

[30] T. Maruyama, A. Ohnishi and H. Horiuchi, Phys. Rev. **C42** (1990) 386; Phys. Rev. **C45** (1992) 2355.

[31] T. Maruyama, A. Ono, A. Ohnishi and H. Horiuchi, Prog. Theor. Phys. **87** (1992) 1367.

[32] K. Niita *et al.*, Phys. Rev. **C52** (1995) 2620.

[33] H. Horiuchi, T. Maruyama, A. Ohnishi and S. Yamaguchi, Preprint KUNS 1028.

[34] A. Ono, H. Horiuchi, T. Maruyama, and A. Ohnishi, Prog. Theor. Phys. **87** (1992) 1185; Phys. Rev. Lett. **68** (1992) 2898; Phys. Rev. **C47** (1993) 2652.

[35] A. Ono, H. Horiuchi and T. Maruyama, Phys. Rev. **C48** (1993) 2946.

[36] T. Maruyama, S. W. Huang, N. Ohtska, G. Li , A. Faessler and J. Aichelin, Nucl. Phys. **B534** (1991) 720; T. Maruyama, G. Li and A. Faessler, Phys. Lett. **B268** (1991) 160.

[37] G. Q. Li, T. Maruyama, Dao T. Khoa, S. W. Huang, Y. Lotfy, G. Li, A. Faessler and J. Aichelin, Z. Phys. **A340** (1991) 721; G. Q. Li, T. Maruyama, Y. Lotfy, S. W. Huang, D. T. Khoa and A. Faessler, Nucl. Phys. **A537** (1992) 631.

[38] Y. Nara, A. Ohnishi and T. Harada, Phys. Lett. **B346** (1995) 217.

[39] High-Energy Reactions Analysis Group, CERN Report CERN-HERA 83-01, 1983 (unpublished).

[40] High-Energy Reactions Analysis Group, CERN Report CERN-HERA 83-02, 1983 (unpublished).

[41] Review of particle Properties, Phys. Rev. **D50** (1994).

[42] J. P. Berge *et. al.*, Phys. Rev. **147** (1966) 945: P. M. Dauber*et. al.*, Phys. Rev. **179** (1969) 1262.

[43] H. Behrend *et. al.*, Phys. Lett. **B56** (1975) 408.

[44] C. M. Ko and B. H. Sa, Phys. Lett. **B258** (1991) 6.

[45] C. W. DeJager, H. De Vries and C. De Vries, At. Data Nucl. Data Tables **14** (1974) 479.

[46] C. J. Horowitz and D. P. Murdock, Phys. Rev. **C37** (1988) 2032.

[47] K. Niita, univ. Giessen preprint (1990); private communication.

[48] T. Fukuda, private communication.

[49] R. E. Chrien, Proceedings of the 23rd INS International Symposium on Nuclear and Particle Physics with Meson Beam in the 1GeV/c Region, (Universal Academy Press, INC. – Tokyo, Japan) p161.

[50] J. Cugnon, P. Deneye and J. Vandermeulen, Phys. Rev. **C41** (1990) 1701.

[51] K. Tsushima, S. W. Huang and A. Faessler, Phys.Lett. **B337** (1994) 245.

[52] P. Koch, B. Muller and J. Rafelski, Phys.Rep. **142** (1986) 167.

Table 1: Branching ratios for Δ^* decay

	J^p	Mass	Width	$N^*\pi$	$N\pi$	$\Delta\pi$	$N\rho$	ΣK	N^* type
P_{33}	$\frac{3}{2}^+$	1.60	0.35	0.15	0.175	0.55	0.125	0.00	$N(1440)$
S_{31}	$\frac{1}{2}^-$	1.62	0.15	0.05	0.25	0.50	0.20	0.00	$N(1440)$
D_{33}	$\frac{3}{2}^-$	1.70	0.30	0.00	0.20	0.40	0.3984	0.0016	
S_{35}	$\frac{1}{2}^-$	1.90	0.20	0.40	0.10	0.05	0.45	0.00	$N(1440)$
F_{35}	$\frac{5}{2}^+$	1.905	0.35	0.00	0.10	0.14998	0.75	0.0002	
P_{31}	$\frac{1}{2}^+$	1.91	0.25	0.60	0.225	0.25	0.15	0.00	$N(1440)$
P_{33}	$\frac{3}{2}^+$	1.92	0.20	0.37	0.20	0.40	0.00	0.03	$N(1440)$
D_{35}	$\frac{5}{2}^-$	1.93	0.35	0.00	0.15	0.00	0.85	0.00	
F_{37}	$\frac{7}{2}^+$	1.95	0.30	0.19	0.40	0.30	0.10	0.01	$N(1689)$

Table 2: Branching ratios for N^* decay

	J^p	Mass	Width	$N\sigma$	$N\pi$	$\Delta\pi$	$N\rho$	$N\eta$	ΛK	ΣK	$N\omega$	$N\eta'$
P_{11}	$\frac{1}{2}^+$	1.44	0.35	0.050	0.65	0.25	0.05	0.00	0.00	0.00	0.00	0.00
D_{13}	$\frac{3}{2}^-$	1.52	0.12	0.049	0.55	0.225	0.175	0.001	0.00	0.00	0.00	0.00
S_{11}	$\frac{1}{2}^-$	1.535	0.15	0.050	0.45	0.05	0.05	0.40	0.00	0.00	0.00	0.00
S_{11}	$\frac{1}{2}^-$	1.65	0.15	0.050	0.70	0.05	0.121	0.01	0.06	0.00	0.00	0.00
D_{15}	$\frac{5}{2}^-$	1.675	0.15	0.009	0.34	0.55	0.09	0.01	0.001	0.00	0.00	0.00
F_{15}	$\frac{5}{2}^+$	1.68	0.13	0.150	0.65	0.10	0.10	0.00	0.00	0.00	0.00	0.00
D_{13}	$\frac{3}{2}^-$	1.70	0.10	0.399	0.10	0.399	0.10	0.00	0.002	0.00	0.00	0.00
P_{11}	$\frac{1}{2}^+$	1.71	0.10	0.015	0.15	0.15	0.125	0.30	0.20	0.6	0.00	0.00
P_{13}	$\frac{3}{2}^+$	1.172	0.15	0.100	0.15	0.10	0.20	0.04	0.05	0.06	0.30	0.00
F_{13}	$\frac{3}{2}^+$	1.90	0.50	0.100	0.15	0.10	0.20	0.04	0.05	0.03	0.63	0.00
P_{13}	$\frac{3}{2}^+$	1.99	0.35	0.100	0.15	0.10	0.30	0.04	0.05	0.03	0.50	0.03
F_{17}	$\frac{7}{2}^-$	2.19	0.45	0.157	0.15	0.11	0.30	0.03	0.003	0.02	0.20	0.02

Table 3: Branching ratios for Λ^* decay

	J^p	Mass	Width	NK	$\Sigma\pi$	$\Lambda\eta$	ΞK	$\Sigma(1385)\pi$	$\Lambda\omega$	$NK(892)$
D_{03}	$\frac{3}{2}^-$	1.52	0.015	0.46	0.43	0.00	0.00	0.11	0.00	0.00
P_{01}	$\frac{1}{2}^+$	1.60	0.150	0.30	0.60	0.00	0.00	0.10	0.00	0.00
S_{01}	$\frac{1}{2}^-$	1.67	0.035	0.20	0.45	0.35	0.00	0.06	0.00	0.00
D_{03}	$\frac{3}{2}^-$	1.69	0.065	0.30	0.40	0.00	0.00	0.45	0.00	0.00
S_{01}	$\frac{1}{2}^-$	1.80	0.300	0.40	0.20	0.00	0.00	0.20	0.00	0.20
P_{01}	$\frac{1}{2}^+$	1.81	0.150	0.33	0.23	0.00	0.00	0.01	0.00	0.43
F_{05}	$\frac{5}{2}^+$	1.82	0.080	0.62	0.14	0.04	0.00	0.12	0.00	0.08
D_{05}	$\frac{5}{2}^-$	1.83	0.095	0.055	0.74	0.02	0.00	0.185	0.00	0.00
P_{03}	$\frac{3}{2}^+$	1.89	0.100	0.35	0.05	0.00	0.00	0.10	0.35	0.15
G_{07}	$\frac{7}{2}^-$	2.02	0.200	0.41	0.23	0.00	0.06	0.20	0.12	0.23
G_{07}	$\frac{7}{2}^+$	2.10	0.200	0.35	0.10	0.03	0.03	0.18	0.001	0.289
F_{05}	$\frac{5}{2}^+$	2.11	0.200	0.20	0.25	0.00	0.00	0.03	0.00	0.56
H_{09}	$\frac{9}{2}^+$	2.35	0.150	0.24	0.20	0.00	0.00	0.26	0.02	0.28
D_{03}	$\frac{3}{2}^-$	2.00	0.200	0.35	0.05	0.05	0.05	0.05	0.15	0.30

Table 4:   Branching ratios for Σ^* decay

	J^p	Mass	Width	NK	$\Lambda\pi$	$\Sigma\pi$	$\Sigma\eta$	ΞK	$\Sigma(1385)\pi$	$\Lambda(1450)\pi$	$\Lambda(1520)\pi$	ΔK	$N\bar{K}(892)$	$\Xi(1530)K$	$\Lambda\rho$
P_{11}	$\frac{1}{2}^+$	1.66	0.10	0.30	0.30	0.30	0.00	0.00	0.00	0.00	0.00	0.05	0.05	0.00	0.00
D_{13}	$\frac{3}{2}^-$	1.67	0.06	0.13	0.15	0.45	0.00	0.00	0.09	0.09	0.09	0.00	0.00	0.00	0.00
S_{11}	$\frac{1}{2}^-$	1.75	0.09	0.31	0.05	0.08	0.41	0.00	0.00	0.00	0.10	0.05	0.00	0.00	0.00
D_{15}	$\frac{5}{2}^-$	1.775	0.12	0.43	0.20	0.05	0.00	0.00	0.12	0.00	0.20	0.00	0.00	0.00	0.00
F_{15}	$\frac{5}{2}^+$	1.915	0.12	0.15	0.20	0.15	0.11	0.04	0.10	0.00	0.00	0.13	0.12	0.00	0.00
D_{13}	$\frac{3}{2}^-$	1.94	0.22	0.20	0.10	0.10	0.10	0.00	0.10	0.20	0.00	0.20	0.05	0.00	0.00
F_{17}	$\frac{7}{2}^+$	2.03	0.18	0.23	0.23	0.10	0.00	0.02	0.10	0.00	0.10	0.20	0.08	0.00	0.00
F_{17}	$\frac{7}{2}^-$	2.10	0.13	0.20	0.20	0.00	0.00	0.00	0.00	0.00	0.00	0.38	0.10	0.00	0.12
D_{15}	$\frac{5}{2}^-$	2.25	0.10	0.10	0.12	0.10	0.10	0.00	0.12	0.00	0.00	0.24	0.12	0.10	0.00
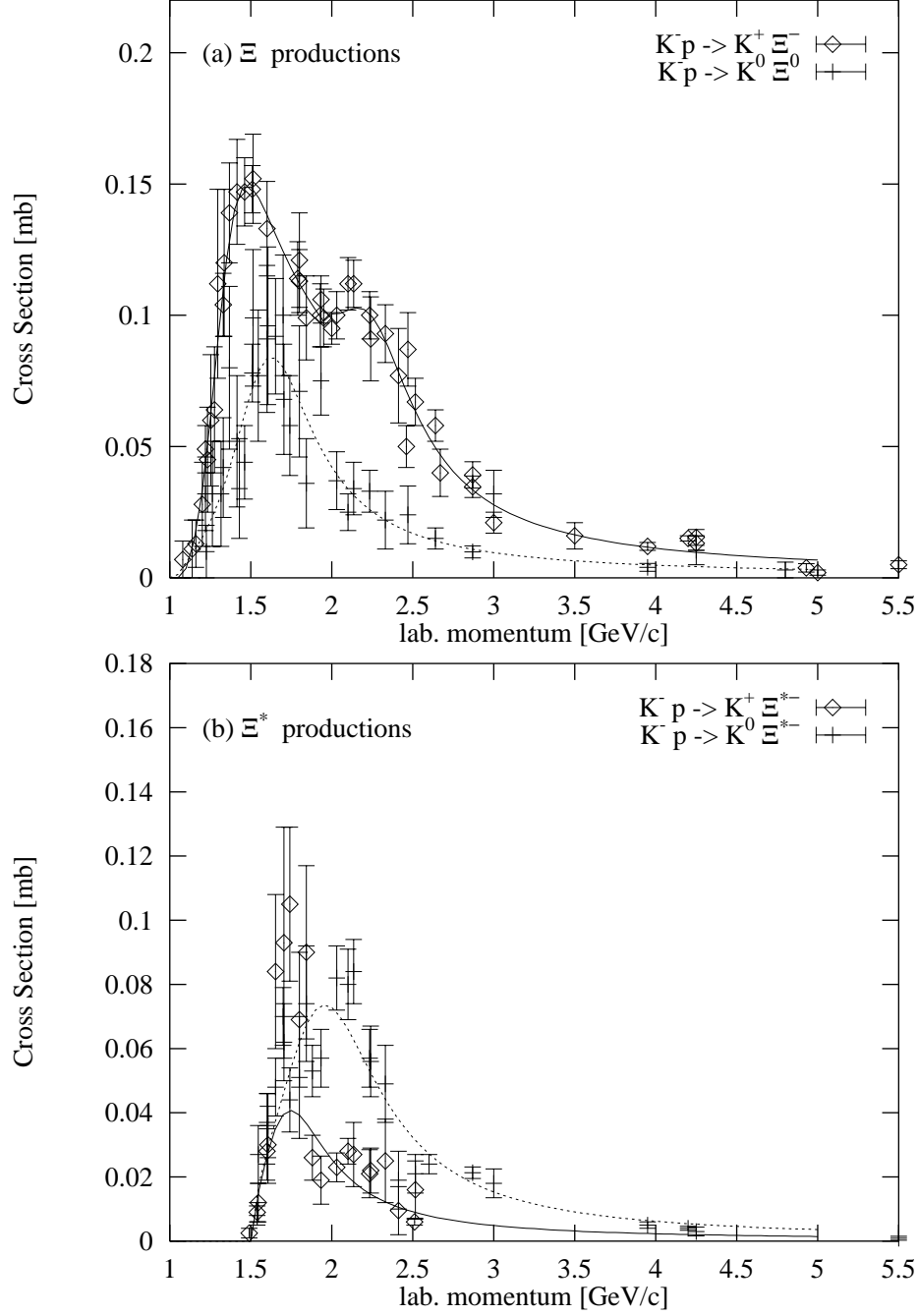
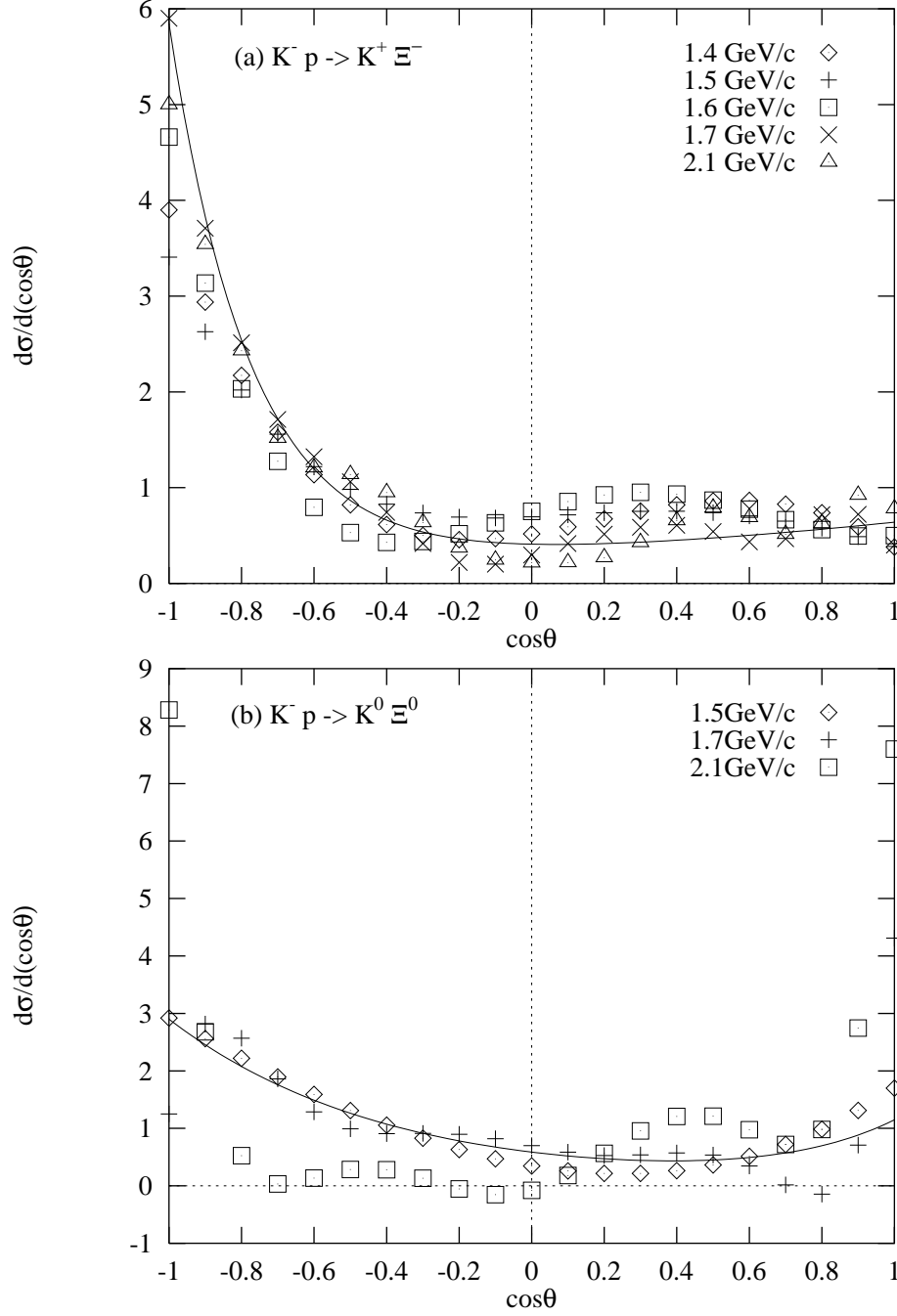Figure 1: Parameterizations of (a)Ξ and (b)Ξ^* production cross sections with experimental data [42].

Figure 2: Angular distributions of (a) $K^- p \to K^+ \Xi^-$ and (b) $K^- p \to K^0 \Xi^0$. The solid curve denotes for the angular distribution parameterized at the laboratory K^- momentum of $p_{K^-} = 1.7 \text{GeV/c}$.
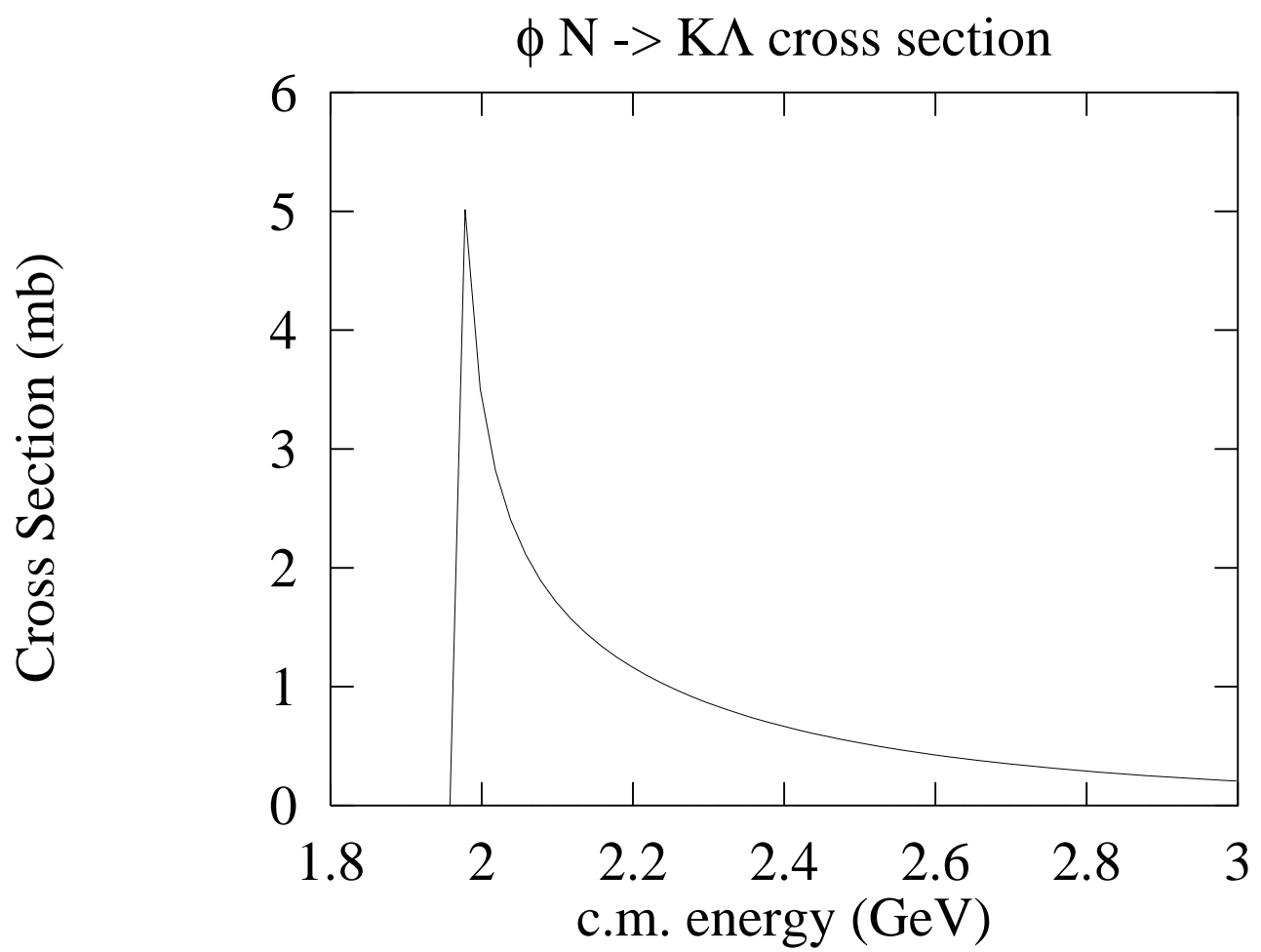
Figure 3: $\phi N \to K\Lambda$ cross section predicted from OBE model of Ref.[44].
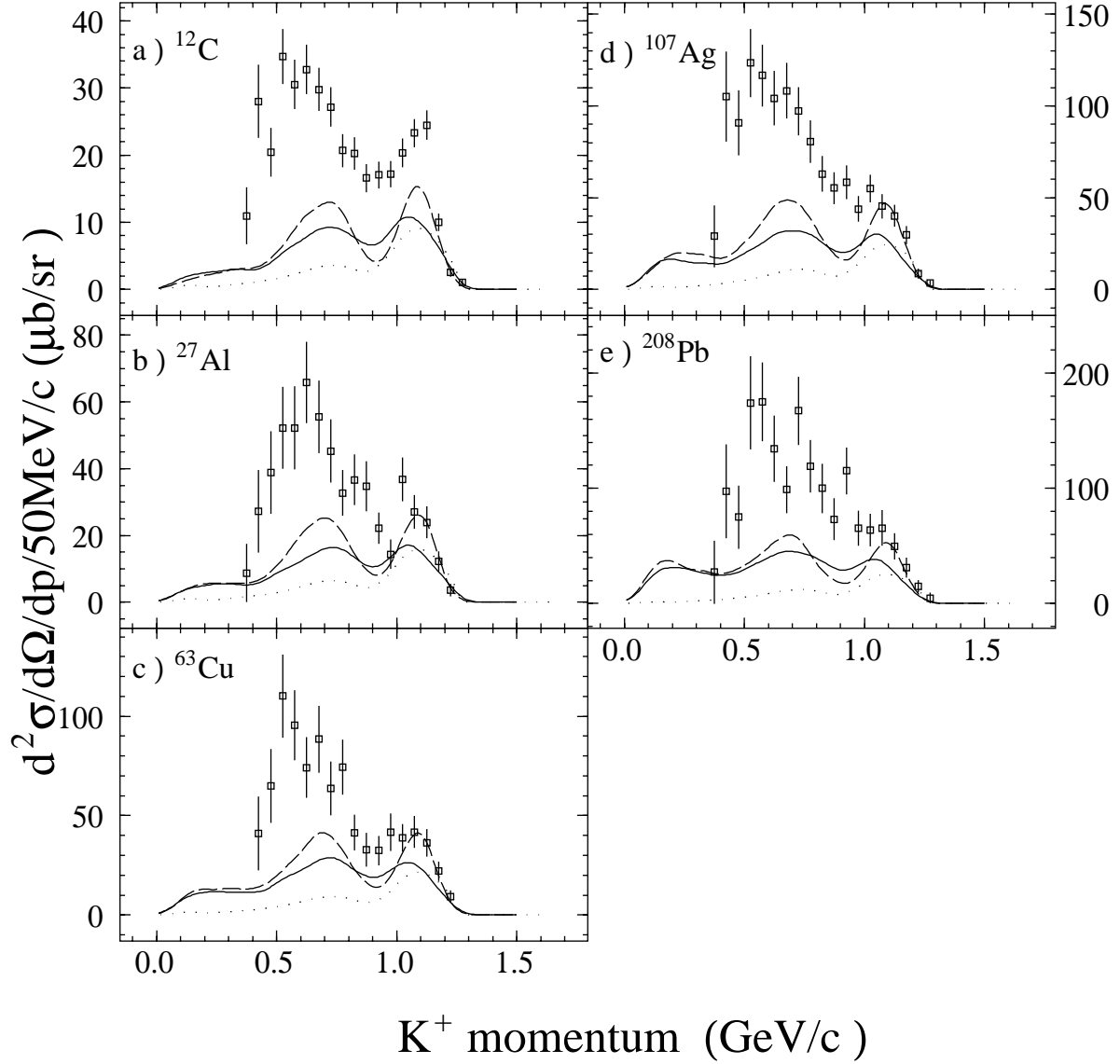
Figure 4: Comparison of the calculated results for the one-step processes (Ξ^- and Ξ^{*-} production) with the experimental data. Solid and dashed lines show the INC results with the matter density and with the Fermi-type density + local Fermi momentum, respectively. Dotted lines show the RIA results with the matter density.
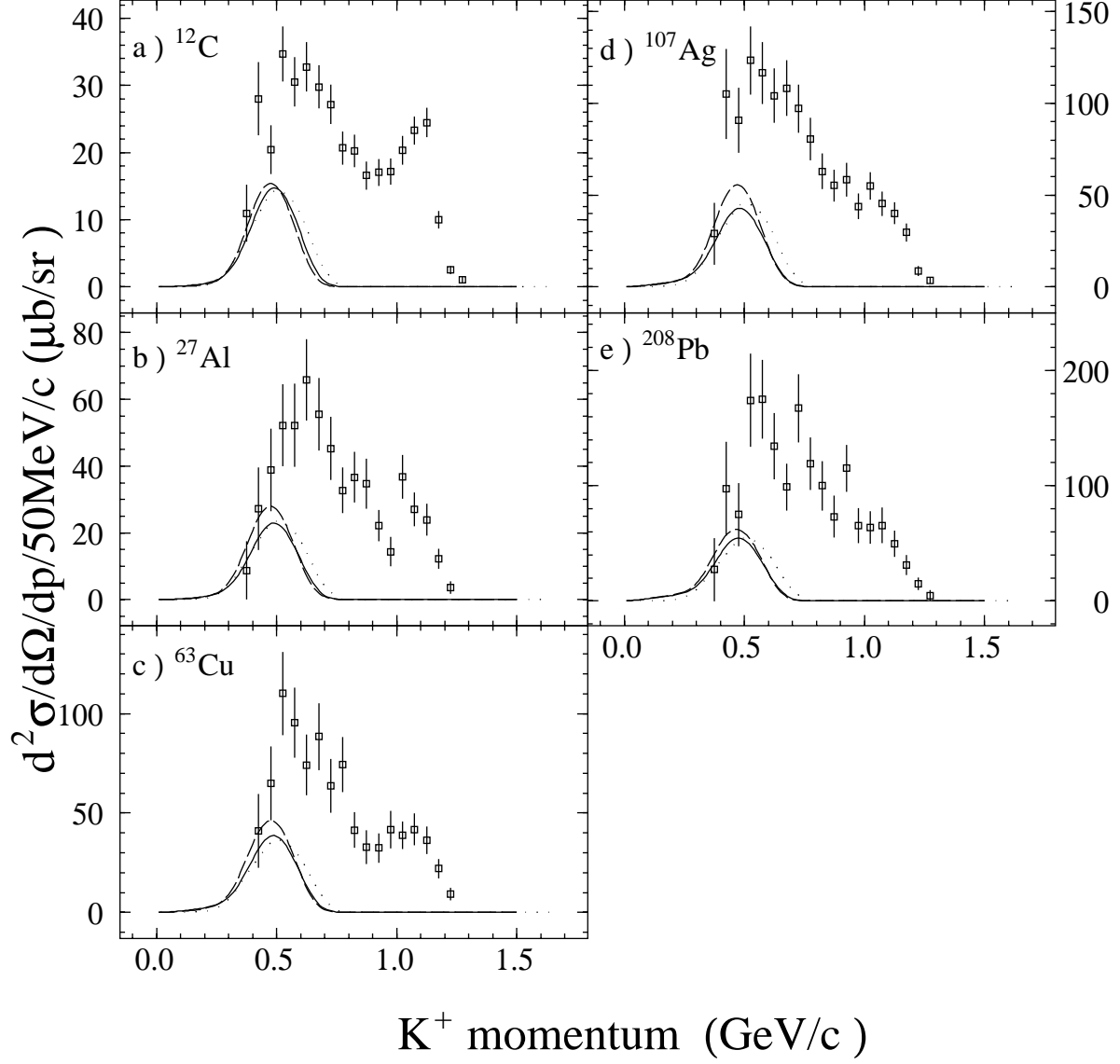
Figure 5: Comparison of the calculated results for the meson-decay($\phi + a_0 + f_0$) contributions to K^+ momentum spectra with the experimental data. Solid and dashed lines show the INC results with the matter density and the Fermi-type density, respectively. Dotted lines show the RIA results with the matter density.
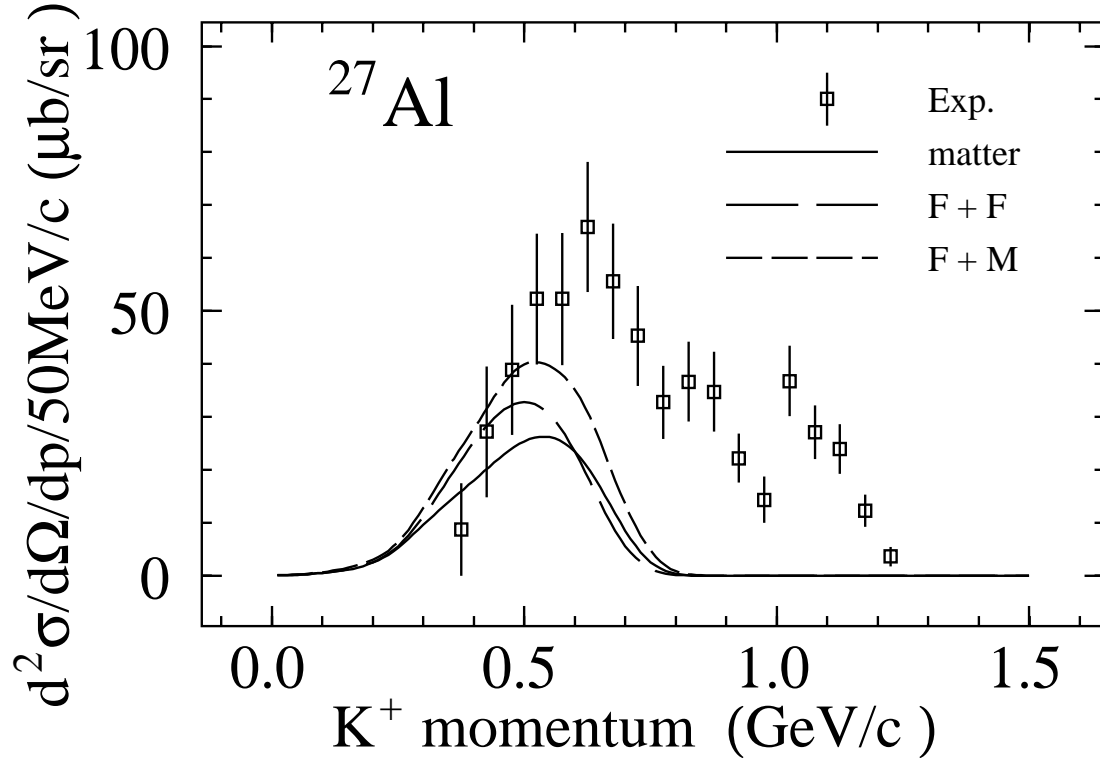
Figure 6: (K^-, K^+) double differential cross sections on ^{27}Al target at $p_{K^+} = 1.65$ GeV/c. The INC calculations only contain ϕ, a_0 and f_0 productions. These spectra are calculated by using matter density (solid line), the Fermi density with the local Fermi momentum (F+F) (long dashed line) and the Fermi density with the matter momentum (F+M) (dashed line).
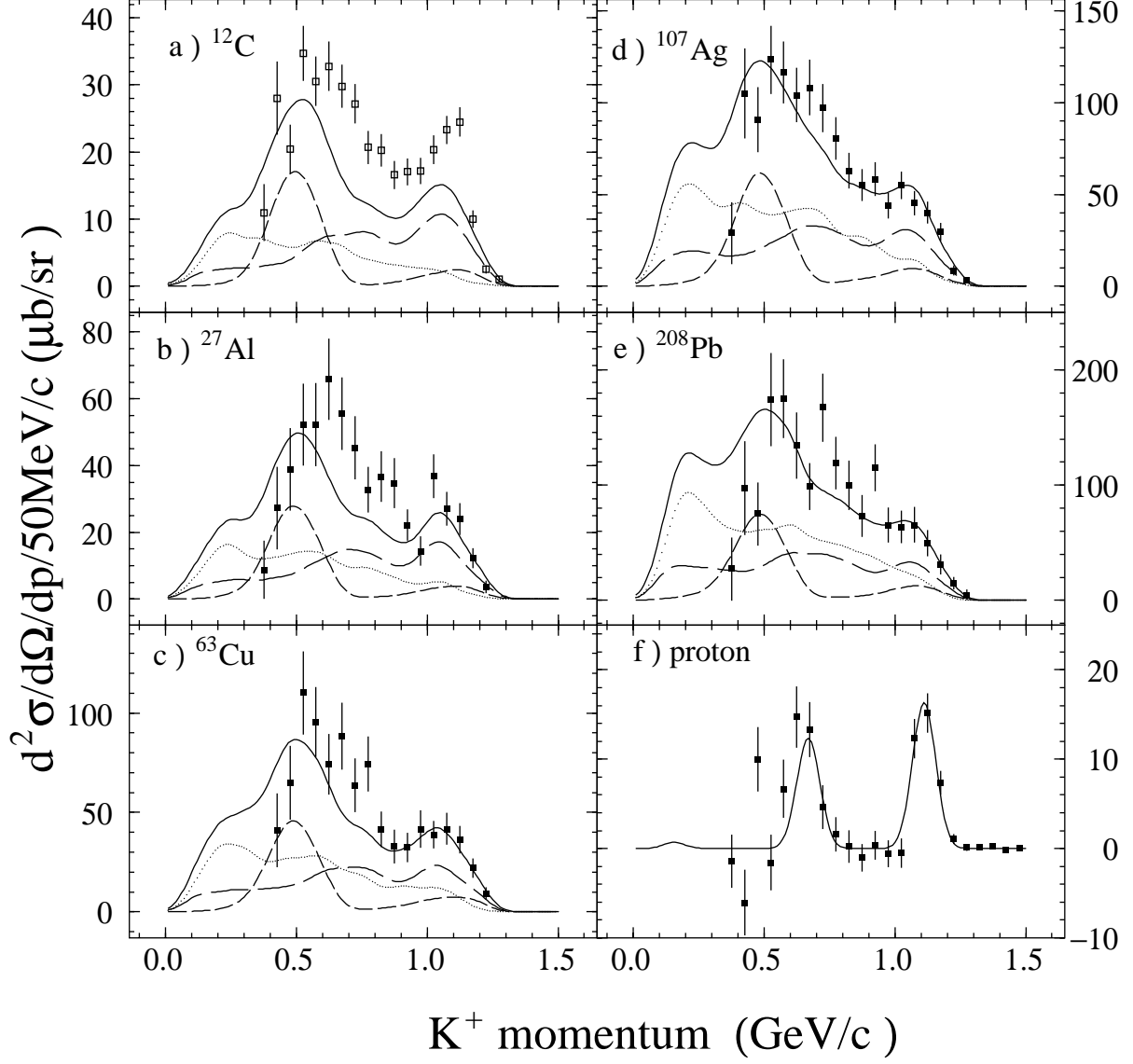
Figure 7: Calculated momentum spectra of K^+ for ^{12}C, ^{27}Al, ^{63}Cu, ^{107}Ag, ^{208}Pb and proton targets at $p_{K^-} = 1.65$ GeV/c using the INC model. The matter density is used. The squares represent the data of Iijima *et al.* [5]. The contributions of Ξ and $\Xi(1535)$ productions are represented by long dashed lines. The dashed and dotted lines correspond to the contributions of ϕ, a_0 and f_0 productions and of two-step processes, respectively. Solid lines denote the results of the total spectrum.
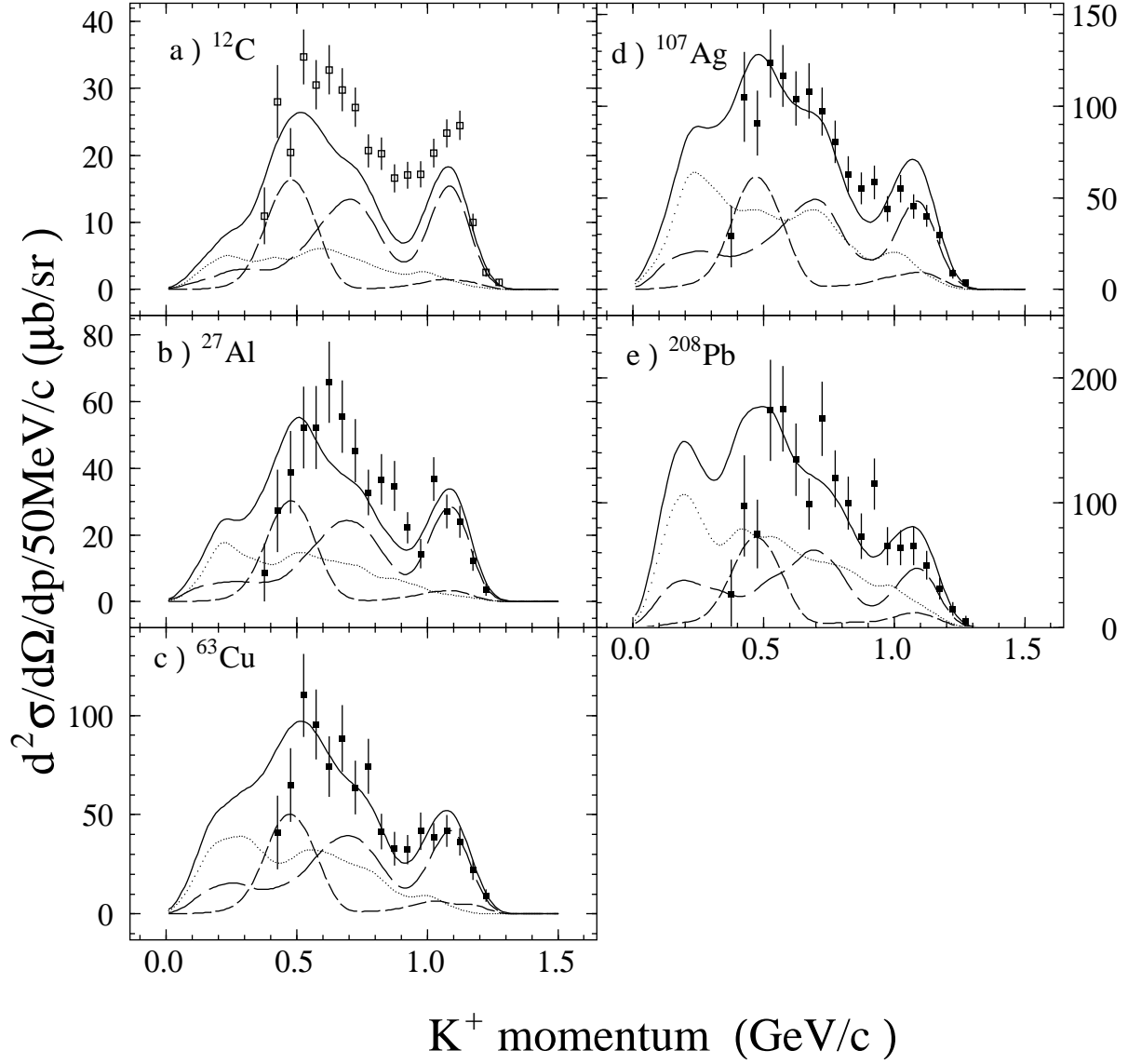
Figure 8: Calculated momentum spectra of K^+ by using the INC model for various targets at $p_{K^-} = 1.65$ GeV/c with the Fermi type density for targets. The notation is the same as fig 7.
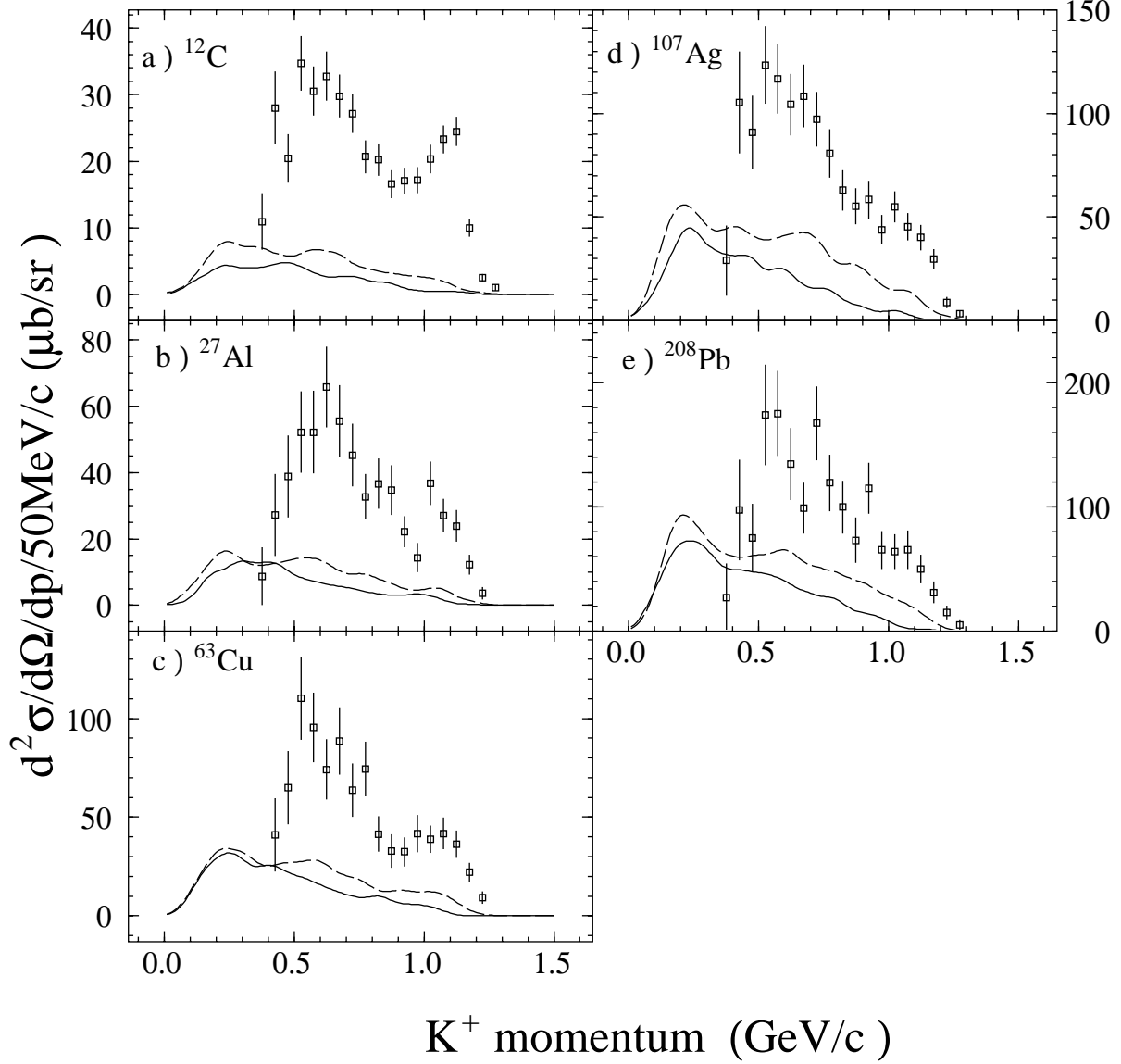
Figure 9: (K^-, K^+) double differential cross sections for only the two-step processes in the INC model, together with the experimental data of Ref. [5]. Solid lines correspond to the results with isotropic angular distribution for the $MN \to K(K^*)Y(Y^*)$, $M = \pi, \rho, \eta, \omega$ and η'. Dashed lines represent the results in which resonance-N angular distributions are equated to those of πN scattering.
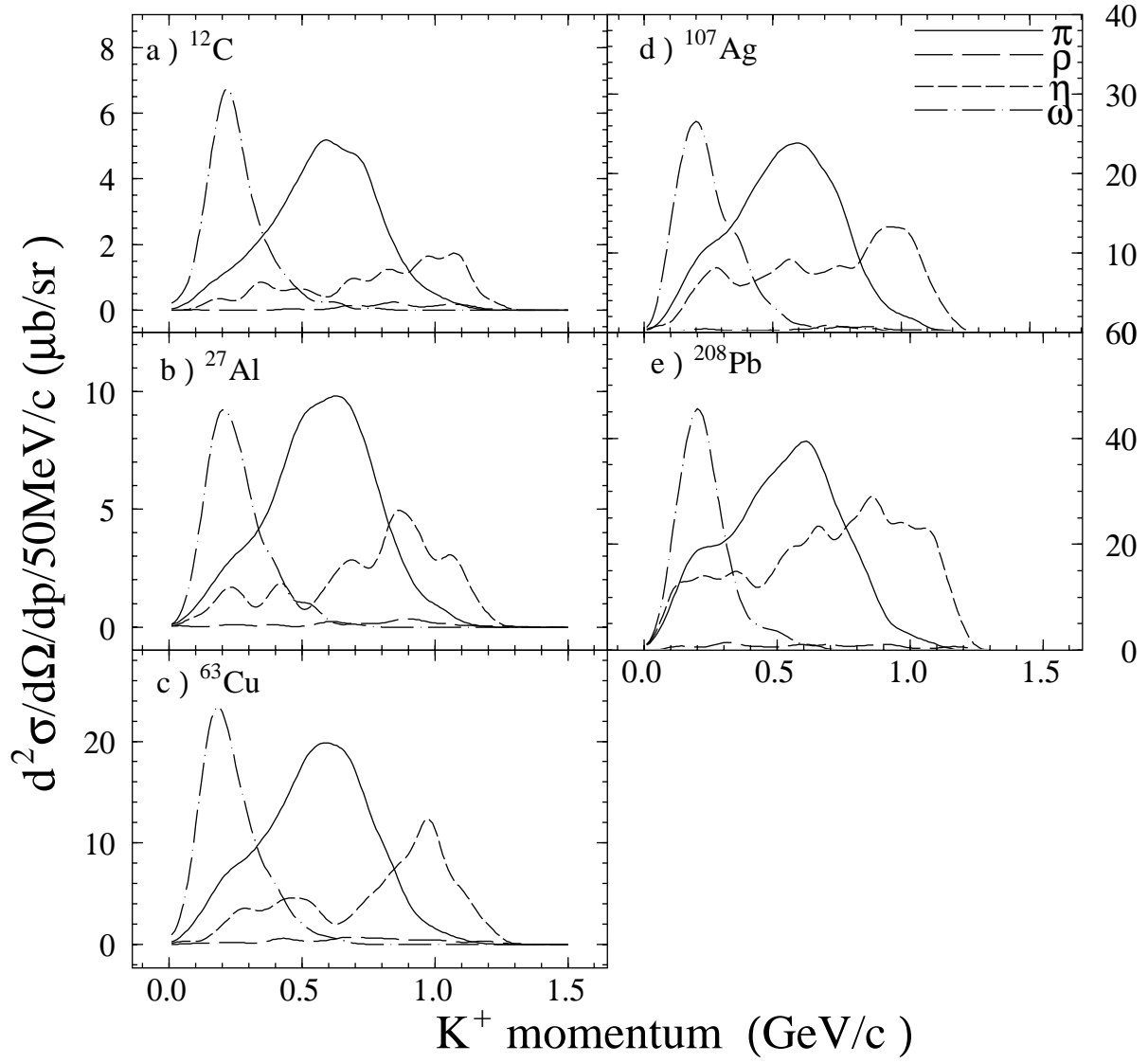
Figure 10: Decomposition of the two-step processes calculated with the INC model. The contribution from π, ρ, η and ω intermediate mesons are represented by solid, long dashed, dashed and dashed-dotted lines, respectively.